Chemical Engineering Journal 506 (2025) 160032

Contents lists available at ScienceDirect

Chemical Engineering Journal

journal homepage: www.elsevier.com/locate/cej

In situ fabricated yttrium doping coatings on aluminum alloy as highly affinity kosmotrope fluorine anti-corrosion surface

Zishuo Ye [a], Shu Xiao [a,*], Yinong Chen [a], Shuyu Fan [a], Yi Wu [a], Fenghua Su [a], Paul K. Chu [b]

[a] School of Mechanical & Automotive Engineering, South China University of Technology, Guangzhou 510641 China
[b] Department of Physics, Department of Materials Science and Engineering, and Department of Biomedical Engineering, City University of Hong Kong, Tat Chee Avenue, Kowloon, Hong Kong, China

ARTICLE INFO

Keywords:
Aluminum alloy
In situ fabrication
Kosmotrope
Yttrium
Fluorine-resistant surface
Density-functional theory

ABSTRACT

Aluminum (Al) alloys have been widely used in semiconductor equipment due to their excellent high specific strength and machinable property. However, the strong electronegativity and high surface charge density in the fluorine environment of process manufacturing tend to result in its poor corrosion resistance performance. Addressing the brittle behavior of fluorides due to strong ionic bonding and the corrosion attack mechanism triggered by the special electronic structure properties of fluoride ions remains a challenge. Studies have indicated that rare earth yttrium (Y) can enhance the fluorine corrosion resistance of ceramic coatings by modifying the fluoride passivation layer structure. In this work, we demonstrate a new strategy for developing high-quality yttrium assisted fluorine corrosion resistant novel coating in situ on aluminum alloy (6061) by two-step micro-arc oxidation (MAO) process. The coatings maintain sustainable corrosion protection and excellent wear resistance performance after 28 days immersion in 0.1 mol/L NaF solution. The results show that the loading of yttrium leads to effectively mitigating the fatal microcracks on the surface by inhibiting the growth of oxygen vacancies in the coatings, and promotes the formation of small sized structures. The stronger and more robust Al-O covalent network structure provides better physical barrier effect and reduces the strong penetration intrusion of small radius fluoride ions. Density-functional theory (DFT) calculations show that matching affinity kosmotrope fluoride ions on the atomic level significantly reduce the adsorption effect on the coating surface. Moreover, yttrium can improve the interfacial dislocation effect of low fracture toughness fluoride reaction film, and effectively inhibit the crack extension of corrosion products as well as promote the stability of corrosion interfacial interaction.

1. Introduction

The 6061 aluminum alloy is widely used in aerospace, automotive manufacturing, semiconductor equipment, and other fields due to its high strength-to-weight ratio, good corrosion resistance and excellent ductility [1,2]. Highly corrosive fluorine compounds are often used in semiconductor manufacturing processes and machine failures due to friction and wear are quite common [3–5]. In front-end and back-end processes, the surfaces of semiconductor equipment are frequently exposed to highly fluorine-corrosive environments and inevitably come into contact with moving parts (e.g. gears, bearings) that create relative motion, which accelerates the wear and tear of the material [6]. Fluoride ions have a small ionic radius and strong chemical permeability, easy to penetrate the medium channel directly to the surface of the protected object forming corrosion. As the integration of semiconductor circuits increases, device equipment becomes more susceptible to defects and damage, which seriously undermines its long-term security and brings tremendous economic losses. Surface modification techniques offer promising solutions to improve their resistance to fluorine corrosion, wear and particle shedding [7].

Understanding the corrosion behavior and failure mechanisms within fluoride corrosion is important for developing strategies to mitigate corrosion issues. Fluoride often presents differentiated passivation breakdown behavior from other halide anions [8]. The strong affinity of fluoride ions stems from their high electronegativity, which exhibits a ‘depolarization reaction’ that disrupts the deceleration process of the electrode reaction and reacts with the oxide film to form halogen salts under strong permeability [9]. Among the halides, small

* Corresponding author.
E-mail address: xiaos@scut.edu.cn (S. Xiao).

https://doi.org/10.1016/j.cej.2025.160032
Received 1 October 2024; Received in revised form 20 December 2024; Accepted 27 January 2025
Available online 28 January 2025

volume fluoride ions have the highest surface charge density and demonstrate the ability to bind surrounding water molecules more strongly than water itself due to hydrogen bonding effects, known as 'kosmotropes'. The Hofmeister lyotropic sequence separates halides into chaotropes (Cl^-, Br^-, I^-) as well as the unique kosmotropes (F^-) [10]. This means that fluoride ions follow the law of matching affinities, where oppositely charged and well hydrated ions are more inclined to attract aggregates and bind to form contact ion pairs [11]. Meanwhile, the strong ion bonds determine that the brittleness is inherent property of the fluoride reaction layer [12]. Special electronic structure properties may allow corrosion behavior in fluorine environments to exhibit significant differences in attack mechanisms. Zhang et al. [13] have reported that the concentration of fluoride ions in solution and pH affect the passivation process of titanium alloys in a fluorine environment. However, the mechanism of fluorine corrosion is still unclear.

Micro arc oxidation (MAO) is often used to generate protective ceramic oxide coatings in situ on valve metals to improve the corrosion and wear resistance of aluminum alloys [14–17]. However, unavoidable micropores and microcracks in the coatings form open channels for the permeation of the corrosive medium [18–20]. Rare earth elements show favorable effects pertaining to grain boundary pinning and grain refinement in ceramic materials [21,22]. Dong et al. [23] have introduced rare-earth elements into high-entropy monociliate coatings to generate more garnet phases and denser layers interspersed with apatite and garnet, resulting in limited penetration of CMAS and improved corrosion resistance. Chen et al. [24] have synthesized HE-$RE_2Sn_2O_7$ ceramic materials with excellent chemical stability by incorporating rare earth elements with different cation radii and masses to achieve lattice distortion, enhance the asymmetry of the structural units, and change the electric dipole moment. Yttrium (Y) is a heavy rare earth element with a small ionic radius, high electrical conductivity, and high ionic activity [25,26]. Ma et al. [27] have refined the grains by adding Al and Y to the Mg-14Li alloy which shows altered MAO growth and thicker coatings with fewer defects. In addition, the yttrium aluminum oxide $Y_xAl_yO_z$ structure has been shown to have better resistance to fluorine attack behavior caused by the formation of stronger Y-F bonds than Al-F bonds after surface fluorination [12]. Therefore, combining MAO with yttrium is expected to generate new exceptional fluorine corrosion resistance functions and properties. Coating growth is closely related to yttrium in the plasma discharge, which is attributed to yttrium salts causing rapid precipitation that affects the stability of the plasma discharge, as well as excess yttrium lowering the overall resistance of the system and making it difficult to reach the threshold for partial discharge leading to growth failure.

This paper aims to design and fabricate yttrium-doped fluorine resistant corrosion coatings on 6061 aluminum alloys in mixed phosphate/silicate solutions with controlled yttrium concentrations by two-step MAO process. Yttrium doping affects the plasma discharge of the coating, reducing its oxygen vacancies and band gap width, decreasing the effectiveness of kosmotropes fluorine adsorption and reducing brittle defects by forming yttrium aluminum oxide structures in fluoride reactive films. The composition, microstructure, corrosion resistance, and wear resistance of the coatings are determined systematically, and the fluorine resistance and mechanism are investigated combined with DFT calculations, with the results providing insights into achieving high durability of aluminum alloy coatings for fields of concern with fluorine corrosive environments.

2. Experimental and calculation details

2.1. Materials

The 6061 aluminum alloy sheet (chemical composition wt%: Si 0.65 %, Fe 0.51 %, Cu 0.24 %, Mn 0.13 %, Mg 1.06 %, Cr 0.11 %, Zn 0.07 %, Ti 0.029 %, and Al balance) purchased from Zhengzhou Mingtai Aluminum Co., Ltd. (Zhengzhou, China) was machined into shapes with dimensions of 40 × 25 × 2 mm^3. Sodium hexametaphosphate ($(NaPO_3)_6$ and molecular weight of 611.77), sodium silicate hydrate ($Na_2SiO_3{\cdot}9H_2O$ and molecular weight of 284.2), and sodium fluoride (NaF and molecular weight of 41.9) were purchased from Sinopharm Chemical Reagent Corporation (Shanghai, China). Yttrium nitrate ($Y(NO_3)_3{\cdot}6H_2O$ and molecular weight of 383.01) was purchased from Shanghai McLean Biochemical Technology Co., Ltd. (Shanghai, China). Homemade deionized water was used, and the reagents were analytical grade.

2.2. Sample preparation

The Al alloy samples were progressively polished with silicon carbide sandpaper (800, 1200, and 2000 grit), degreased ultrasonically in alcohol for 10 mins, and dried in air. Micro-arc oxidation was conducted using the AC bipolar 11 KW micro-arc oxidation power supply (DOP-B, Plasma Technology Ltd., China). During MAO, the pulse frequency, positive/negative duty cycle, and deposition time were 600 Hz, 20 %, and 11 mins. The anode was an aluminum alloy, and the cathode was the stainless-steel electrolytic bath. MAO was conducted in the constant current mode with a forward current of 1 A/dm^2 in two stages, pretreatment in the electrolyte composed of 35 g/L $(NaPO_3)_6$ and 4 g/L Na_2SiO_3 for 210 s to form the passivation oxide and then in electrolytes containing 35 g/L $(NaPO_3)_6$, 4 g/L Na_2SiO_3, and different concentrations of $Y(NO_3)_3$ (0, 1.5, 2.0, 2.5, and 3.0 mol%/L) for 450 s (samples designated as Al/MAO-0/1.5/2.0/2.5/3.0 mol%/L, respectively). The temperature was kept at 25 °C by circulation. After MAO, the samples were rinsed with deionized water and dried naturally.

2.3. Characterization

The surface morphology and elemental composition were characterized by field-emission scanning electron microscopy (SEM, SU8200) and energy-dispersive X-ray spectroscopy (EDS, X-Max20) after thin Au films were deposited on the sample to alleviate charging. The microstructure and composition of the coatings and corrosion products were determined by high-resolution transmission electron microscopy (HR-TEM, JEM-3200FS, JEOL), grazing-incidence X-ray diffraction (GIXRD, Smartlab with Cu K_α X-ray) in steps of 0.02° in the 2θ range from 10° to 85°, and X-ray photoelectron spectroscopy (XPS, ESCALAB 250Xi, Thermo Fisher Scientific, USA) referenced to the C 1 *s* peak at 284.8 eV and fitted by the Advantage software. The porosity was calculated by the Image J software for separate tests, and the DDS-11A (Shanghai, China) was used to measure the conductivity of the electrolytes. Each test was conducted on three samples/locations to improve the statistics.

2.4. Wear resistance evaluation

The wear test was carried out before and after immersion in 0.1 mol/L sodium fluoride at room temperature and relative humidity of 25 ± 3 °C and 50 ± 3 % RH in the rotational mode using the ball-on-disk tribometer (UMT-Tribolab, Bruker). The friction pairs were aluminum oxide (ball diameter of 6 mm) and the Al, Al/MAO, and Al/MAO-Y samples. The dry friction test was conducted in a dry environment at an average speed of 200 rpm at a load of 2 N for 30 mins and a wear radius of 5 mm. The wear tracks and wear areas were observed by three-dimensional optical profilometry (RTEC UP Dual Mode, USA). All the tests were conducted thrice (n = 3) to generate averages. After testing, the samples were characterized by SEM and EDS, and the wear rates were derived by Eq. (1) [28]:

$$W = \frac{V}{S \bullet F} = \frac{2\pi RA}{S \bullet F}, \quad (1)$$

where R (mm), A (mm^2), S (m), and F (N) are the wear radius, wear area, wear distance, and load, respectively.

2.5. Corrosion resistance assessment

Electrochemical tests were carried out with the Gamry Framework software on the electrochemical workstation (Gamry, Reference 600+, USA) with the conventional three-electrode cell comprising samples connected as the working electrode, saturated calomel electrode (SCE) connected as the reference electrode, and platinum plate connected as the counter electrode in a Faraday cage. The open circuit potential (OCP), potentiodynamic polarization (PDP), and electrochemical impedance spectroscopy (EIS) tests were carried out in 50 ml of 0.1 mol/L sodium fluoride using an exposed area of 1 cm^2. Before the electrochemical tests, the specimens were immersed in the solution for at least 30 min to establish a stable OCP. PDP tests were performed from −500 mV to + 500 mV (vs. E_{ocp}) at a scanning rate of 1 mV/s. The corrosion potentials (E_{corr}) and current densities (i_{corr}) were obtained by Tafel extrapolation. Electrochemical impedance spectroscopy was performed in 0.1 mol/L sodium fluoride for 12, 24, 48, and 72 h from 100 mHz to 100 kHz with 15 mV sinusoidal perturbation. The EIS spectra were analyzed by the Gamry Echem Analyst and the most appropriate equivalent circuit (EC) model was derived. The samples were immersed in 0.1 mol/L sodium fluoride solution for a total of 28 days and were observed on the 3rd, 7th, 18th, 24th, and 28th days. All micro-arc oxidized samples were sealed with epoxy resin at the contact point with the connected power source prior to immersion testing, preventing corrosion and diffusion from occurring preferentially in this area. Surface morphology and elemental composition of specimens corroded by immersion for 28th days were characterized by SEM and EDS. All the electrochemical and immersion tests were performed at room temperature and three samples were analyzed to generate averages.

2.6. First-principles calculations

First-principles calculations were performed using the density-functional semi-core pseudopotential method implemented in the DMol3 package [29]. The general gradient approximation (GGA) of the Predew-Burke-Ernzerhof (PBE) formula was used for the exchange–correlation function, with a customized approach from Grimme to account for dispersion effects considering the spin-polarization effects [30,31]. The optimization process continued until the self-consistent field (SCF) convergence tolerance, atomic force, maximum displacement, and total energy were reduced to less than 1×10^{-6} Ha, 2×10^{-3} Ha/Å, 5×10^{-3} Å and 1×10^{-5} Ha/atom, respectively. The bulk and surface model of α-Al_2O_3 was developed with optimized Al_2O_3 cells (a = b = 4.80503 Å). To avoid layer-to-layer interactions under periodic boundary conditions, a vacuum layer above 10 Å was added and a 3 × 3 × 1 k-mesh was used. The structure was fully optimized to achieve stability before the next calculation.

In the process of the coating growth, the electrical conductivity of the coating and the degree of oxidation play a significant role in the discharge. We replaced the same position of Al with Y and the same position of oxygen vacancies were also taken into account to jointly measure the effect of coating properties on the discharge characteristics. The crystal structure models with and without Y-substitution were YAlO and AlO (without oxygen vacancies) and YAlO/O_{vac} and AlO/O_{vac} (with oxygen vacancies). The elastic modulus was calculated by the constant strain mode to illustrate the wear properties. During the corrosion process, F^- adsorbed onto the coating surface to destroy it gradually, which is an accumulation of temporal factors. Reducing the frequency of contact between F^- and the coating is considered to be one of the important means of corrosion resistance. Hence, a surface adsorption model in solution environment was constructed to assess the adsorption stability of F^- under simulated experimental conditions. The solvation model was employed to simulate the aqueous environment, in which 78.54 was the water dielectric constant. In order to avoid surface interactions from charge aggregation, a dipole slab correction was applied. The atom type symbol X_p^n shows the element (X = Al, O, Y), the number of surface layers (p = 1, 2, 3, 4), and the positions of the atoms in the region (n = 1, 2, 3, 4, 5, 6). Refer to Supporting Material Fig. S5 for the precise location of the atomic layer symbols.

The adsorption energy (E_{ads}) of F^- on clean surfaces corresponds to the structure and the stability of adsorption is calculated by Eq. (2) [32]:

$$E_{ads} = E_{substrate/F^-} - E_{substrate} - E_{F^-}, \quad (2)$$

where $E_{substrate/F^-}$, $E_{substrate}$, and E_{F^-} are the energies of the system, substrate, and fluoride ions. The oxygen vacancy formation energy ($E_{O_{vac}}$) indicating the energy required for the formation of oxygen vacancies during growth was calculated by Eq. (3) [33]:

$$E_{O_{vac}} = E_{Y_xAl_{2-x}O_{3-y}} + \frac{1}{2}E_{O_2} - E_{Y_xAl_{2-x}O_3}, \quad (3)$$

where $E_{Y_xAl_{2-x}O_{3-y}}$, E_{O_2}, and $E_{Y_xAl_{2-x}O_3}$ are the energies of the system with an oxygen vacancy, gaseous O_2, and pure system without vacancies. The charge groups, bond length, and density of state (DOS) were calculated to characterize the covalent interactions.

3. Results and discussion

3.1. Plasma discharge characteristics

Fig. 1a shows the discharge voltage versus time curves in electrolytes with different Y^{3+} concentrations divided into three regions. As time increases, the build-up of insulating oxides on the surface of the sample increases leading to a constant increase in voltage with time. In the initial stage 1 (anodic oxidation), the ion current density is an important component of the overall current density, and the electric field provides an electric potential for the transport of cations and anions in the electrolyte. The aluminum alloy is oxidized quickly under the action of the electric current, forming a potential barrier (dense passivation layer), and the reactive ions in the electrolyte accumulate in the passivation layer, causing the anodic voltage to rise sharply [34]. In stage 2 (spark discharge stage), the thickness of the oxide film increases gradually. When the actual transient voltage reaches the breakdown voltage of the insulating dielectric layer, the avalanche current contributes to the breakdown of the anode film and the coating begins to discharge. In stage 3 (micro-arc discharge stage), the voltage stabilizes. The alkaline electrolyte is replaced by the yttrium-containing electrolyte and the surface charge of the coating is re-collected. The higher the concentration of yttrium nitrate in the solution, the smaller the slope of the curve, as the discharge voltage decreases gradually with Y^{3+} concentration. The final voltages for the 0, 1.5, 2, 2.5, and 3 mol%/L solutions at 660 s were 622, 574, 556, 540, and 535 V, respectively, because Y^{3+} increases the conductivity of the electrolyte (Fig. 1b), leading to a decrease in the discharge voltage in agreement with the equation by Burger and Wu [35].

Fig. 1c depicts the photographs of the transient discharge of Al/MAO-0 mol%/L Y^{3+} and Al/MAO-2.5 mol%/L Y^{3+} during MAO at different time points. The samples are immersed in the pretreatment electrolyte in the time range of 0–180 s. Arcing becomes gradually apparent with time, which corresponded to the pattern of voltage distribution and afterward, the electrolyte enters the oxide layer through the discharge channels, resulting in a large number of white micro-electrical sparks moving rapidly across the sample surface. The distribution of sparks in the central region at 180 s is denser on account of the fringe effect of the electric field causing the electric power lines on the surface to be unevenly distributed in different areas, so the current passes through the region with a small bending radius. The growth in the edge regions is higher than that in the center region, leading to the decomposition of weak alumina at the edge. The micro-discharge spreads from the corners and edges to the whole surface and concentrates in in the central region [36]. The samples are immersed in the yttrium-containing electrolyte for 210–660 s. During process II, sparks

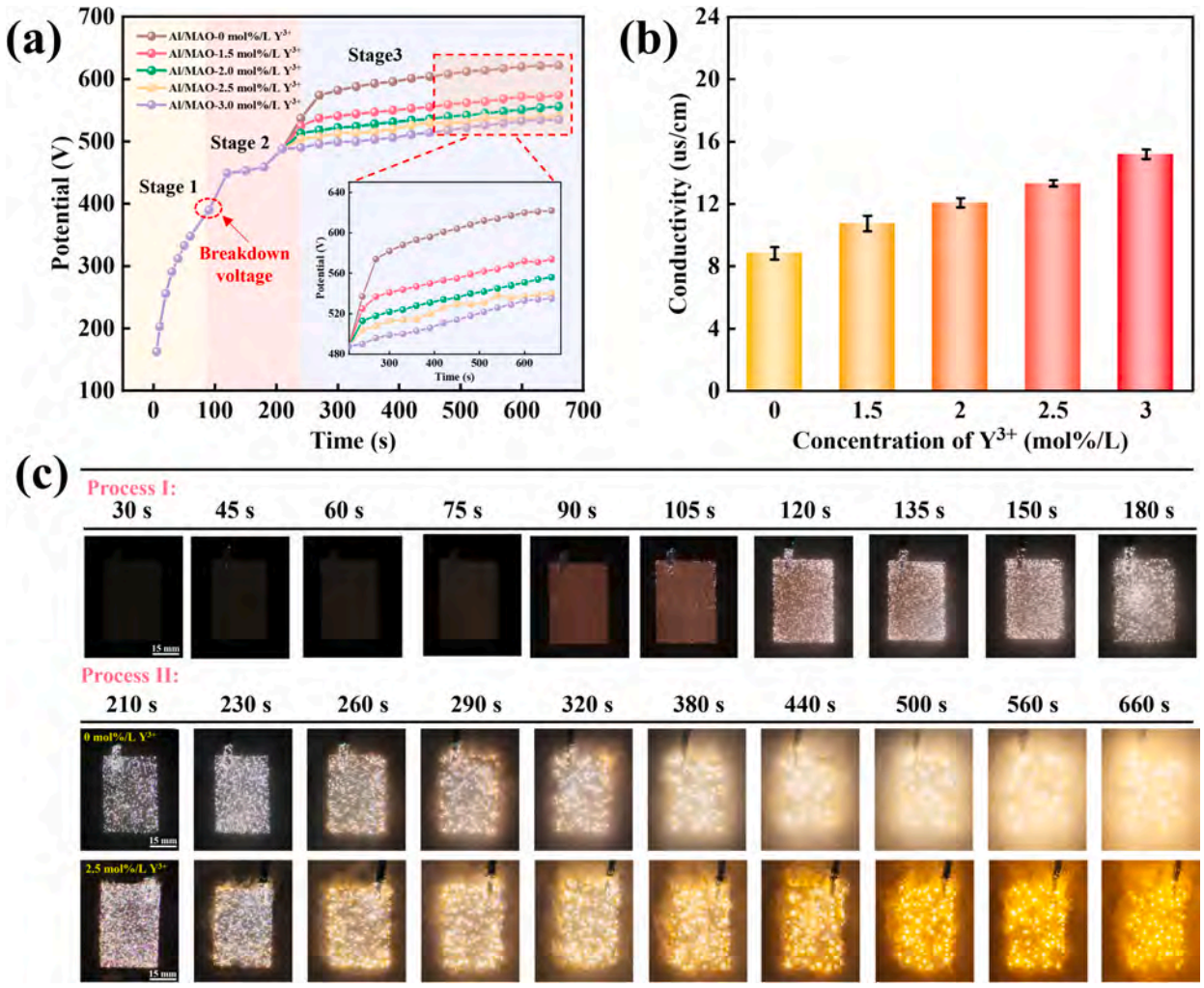

Fig. 1. Electrolytes with different concentrations of Y^{3+}: (a) Voltage versus time for MAO coatings; (b) Conductivity; and (c) Plasma discharge morphology: Process I (pretreatment stage) and Process II (formal treatment stage with different Y^{3+} concentrations).

become more pronounced as the time increased changing from white to orange due to the emergence of arcs and the strong gas escape (320 s). As time elapses, dielectric breakdown is more frequent, and the gas is released rapidly while the arc discharge becomes increasingly violent. The distribution of the arc spot changes from sparse to compact, and the sparks coalesce into larger sparks to melt wrapping the whole alloy gradually. Throughout the process, the arc point continuously moves rapidly over time. It is interesting that the Y^{3+} electrolytes show yellow arcs earlier (230 s), but the lifetime and intensity in the central region are reduced, showing an orange uniform discharge surface and large sparks changing into fine ones.

3.2. Morphology and chemical composition

Fig. 2(a-e) show the SEM images of the samples prepared with different Y^{3+} concentrations, revealing a porous structure with air holes and microcracks of different sizes typical of MAO coatings. The formation of micro-cavities is linked to the generation of magma-like molten oxides and the ejection of bubbles from the discharge channels. These cavities are channels for oxidation, but they are not interconnected [37]. The plasma moves along the strong electric field direction and the porous structure shrinks after the arc is extinguished to form the typical volcano-like features in the MAO coatings [38]. Micro-cracking is associated with internal stresses arising from the micro-array plasma discharge during rapid solidification.

Fig. 2g shows the average porosity and pore size distribution. The average porosity decreases from 3.46 ± 0.2 % (Al/MAO-0 mol%/L Y^{3+}) to 1.093 ± 0.12 % (Al/MAO-2.5 mol%/L Y^{3+}). With increasing electrolyte conductivity, the energy required for ion migration decreases, and then the energy provided by the external power supply was mainly used for the coating formation resulting in higher energy efficiency. The average pore size decreases from 2.262 ± 0.4 to 1.25 ± 0.18 μm. However, if the concentration of Y^{3+} is high, the porosity increases and the standard deviation of the mean pore size becomes higher, with greater dispersion of the pore size distribution due to insufficient discharge and the inability of the molten oxide to backfill the pores in time [39]. Fig. 2(a_2) shows the crack in the Al/MAO-0 mol%/L Y^{3+} ceramic coating, in which the connected cracks become short-circuit channels for corrosive ions accelerating the corrosion damage of the substrate. By adding Y^{3+}, the cracks become shorter and more isolated and scattered, which is positive for the corrosion resistance. The results show that Y^{3+} doping modifies the surface morphology and micropore size.

Fig. 2f shows the elemental concentrations of the samples prepared with different Y^{3+} concentrations. Al, O, Si and P are typical elements for the preparation of MAO coatings from mixed silicate and phosphate electrolytes. The Y concentration increases to 7.71 % (Al/MAO-3.0 mol %/L Y^{3+}), but that of Al decreases from 37.42 % to 27.76 %, and that of O does not change significantly, confirming that Y replaces Al in the lattice. In addition, the cross-sectional SEM and EDS elemental scans

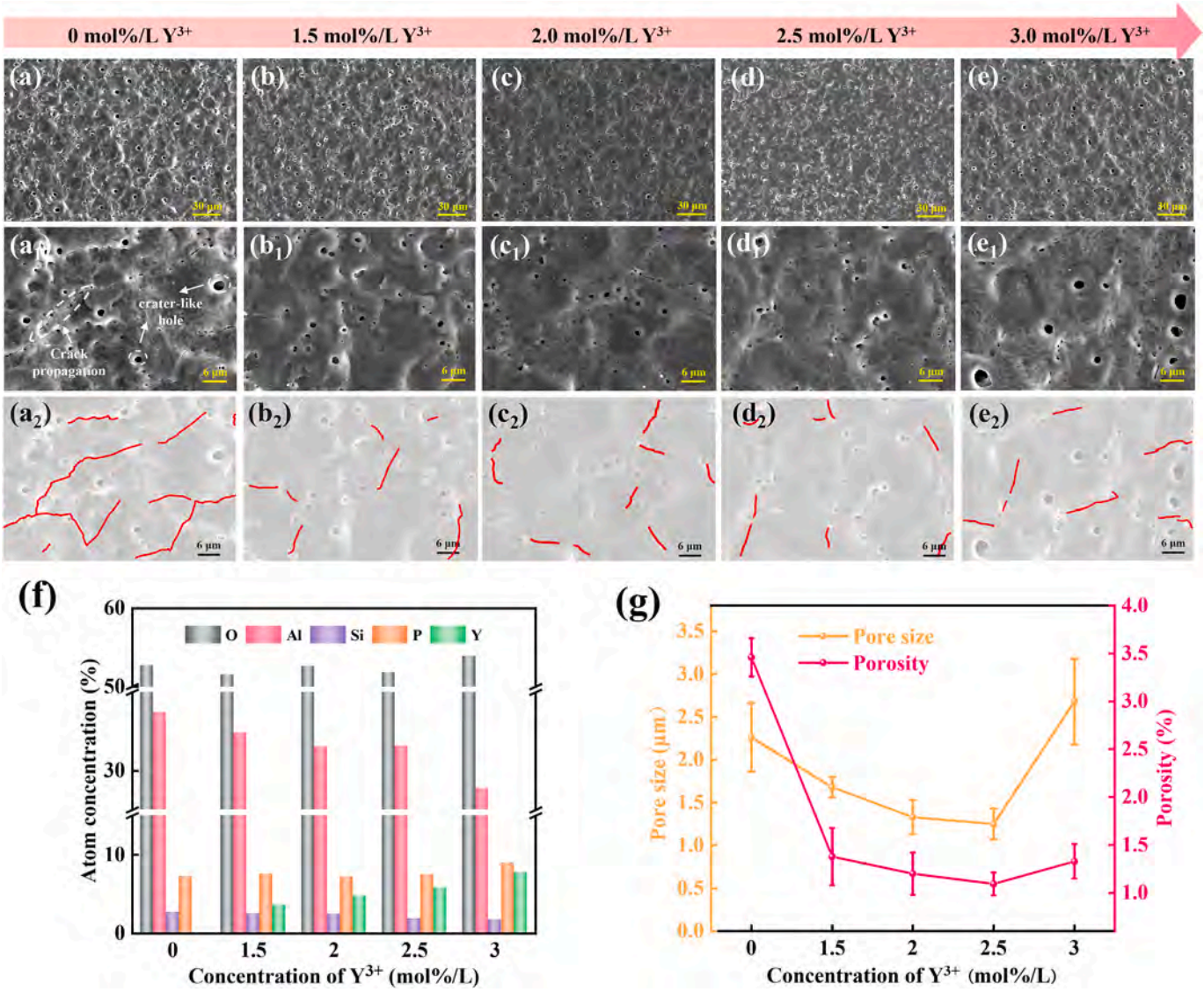

Fig. 2. SEM surface images of MAO coatings with different Y^{3+} concentrations: (a) 0 mol%/L; (b) 1.5 mol%/L; (c) 2.0 mol%/L; (d) 2.5 mol%/L; (e) 3.0 mol%/L; SEM images at high magnification: **(a_1-e_1)**; Surface cracks at high magnification: **(a_2-e_2)**; Coatings prepared with different concentrations of Y^{3+}: (f) Elemental atomic concentrations; (g) Average pore size and porosity.

reveal that the coating thickness is increased when the Y^{3+} concentration is 2.5 mol%/L (Fig. S1).

In order to investigate the chemical composition of the coatings and to further demonstrate the doping of Y^{3+} in the coatings, XPS analyses were carried out on the two micro-arc oxidation coatings prepared to obtain information on the outermost regions. Fig. 3 shows the survey XPS spectra as well as the Al 2*p*, O 1 *s*, C 1 *s*, Y 3*d*, Si 2*p*, and P 2*p* spectra. The characteristic peaks of Y 3*d* indicate that the elemental Y involved in the coating reaction into the coatings during MAO process, where the elemental C may be derived from the organic matter exposed to the air. The binding energy of the Al 2*p* peak is 73.8 eV (Fig. 3b), indicative of Al_2O_3 [40]. For the high-resolution energy spectra of O 1 *s*, it can be observed that both coatings show aluminum oxide corresponding diffraction peaks at 530.8 eV and 530.7 eV (Fig. 3c), the difference is that the Y-doped coating shows the Y-O diffraction peaks at 531.7 eV, which corresponds to the high-resolution energy spectra of Y 3*d* [41]. The Si 2*p* spectrum shifts to a higher binding energy after Y doping (Fig. 3e). Fig. 3f shows the P 2*p* spectra revealing binding energies of 133.18 eV and 133.38 eV, respectively. Ji et al. [42] have investigated P-modified MAO aluminum alloy with the $AlPO_4$ phase showing $[PO_4]^{3-}$ at 132.5–135.0 eV, suggesting that P is derived from sodium hexametaphosphate and present in the form of $[PO_4]^{3-}$, perhaps $AlPO_4$. The Y 3*d* spectra in Fig. 3d show binding energies of 152.7, 157.7, 159.6, and 160.1 eV. The binding energy of 157.7 eV ($3d_{5/2}$) is related to Y-O in Y_2O_3 at 156.8 eV, and that of 159.6 eV ($3d_{3/2}$) corresponds to Y-O in the $Y(OH)_x$ peak at 159.09 eV [43,44]. The chemical shift ($\Delta = EB\_Y^{3+}_{5/2} - EB\_Y^{0}_{5/2}$) indicates that Y has the trivalent state in the alumina coating [45]. The results show that the main phase of Al_2O_3 is substituted with Y.

3.3. Electrochemical evaluation

In order to evaluate the effects of Y doping on the fluorine corrosion resistance of MAO coatings, electrochemical tests are performed on the substrate and different Y-doped coatings. Table 1 and Fig. 4 show the dynamic potential polarization results together with the corresponding corrosion currents and corrosion potentials after immersion in 0.1 mol/L NaF for 30 mins. Generally, the corrosion current density (i_{corr}) is used as a direct indicator of the susceptibility of the materials to corrosion, and there is an inverse relationship between i_{corr} and corrosion resistance

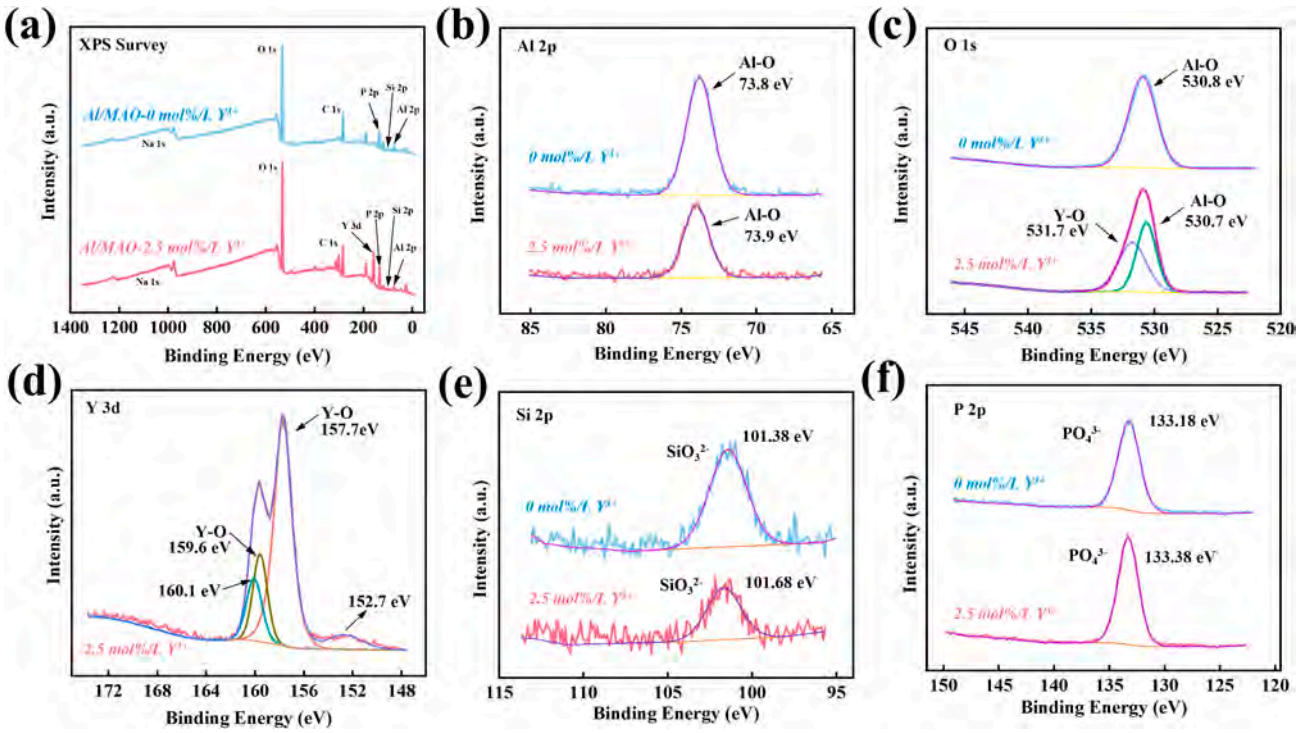

Fig. 3. XPS spectra (a) Survey, (b) Al 2*p*, (c) O 1 *s*, (d) Y 3*d*, (e) Si 2*p*, and (f) P 2*p*.

Table 1
Potentiodynamic polarization parameters in 0.1 mol/L NaF.

Sample	I_{corr} (A/cm^2)	E_{corr} (V/SCE)
substrate	$(2.53 \pm 1.21) \times 10^{-5}$	-1.226 ± 0.05
0 mol%/L Y^{3+}	$(7.25 \pm 0.98) \times 10^{-8}$	-0.824 ± 0.07
1.5 mol%/L Y^{3+}	$(3.17 \pm 0.88) \times 10^{-8}$	-0.757 ± 0.04
2.0 mol%/L Y^{3+}	$(2.07 \pm 0.39) \times 10^{-8}$	-0.839 ± 0.06
2.5 mol%/L Y^{3+}	$(4.49 \pm 0.96) \times 10^{-9}$	-0.784 ± 0.03
3.0 mol%/L Y^{3+}	$(6.03 \pm 1.49) \times 10^{-8}$	-0.946 ± 0.06

[46]. The corrosion potential (E_{corr}) which indicates the chemical stability of the sample in the corrosive medium is combined with i_{corr} to analyze the corrosion kinetics. Fig. 4a shows that E_{corr} moves in the positive direction and i_{corr} moves in the negative direction with increasing Y^{3+} concentrations, indicating that Y doping can retard the penetration of fluorine in the corrosive medium to the substrate. A smaller i_{corr} represents weaker fluoride ion adsorption and stronger corrosion resistance [47]. The pristine 6061 aluminum alloy shows the worst corrosion resistance manifested by the smallest corrosion potential (−1.226 V) and the biggest corrosion current (2.53×10^{-5} A/cm^2). However, after MAO, the corrosion current density decreases significantly and the corrosion potential increases to −0.824 V, which indicates a reduction in the tendency of corrosion initiation due to thermodynamics. E_{corr} of Al/MAO-2.5 mol%/L Y^{3+} is 0.784 V and i_{corr} is 4.49×10^{-9} A/cm^2, representing about 6.5 % of the undoped Y^{3+} and 0.02 % of the 6061 substrate, suggesting its better fluorine corrosion resistance. However, excessively high concentrations cause the corrosion current to increase. This is attributed to the enhanced coating growth facilitated by the addition of appropriate amounts of Y^{3+}. However, when the Y^{3+} content in the solution continued to increase, the high conductivity resulted in the breakdown of its anodic passivation film becoming difficult and the plasma discharge being inadequate, which resulted in the coating's surface defects increasing and thickness decreasing at high concentrations of Y^{3+} (Fig. S2), showing poor fluorine corrosion resistance performance. The results show that the addition of Y^{3+} reduces the pore size and porosity while improving the shielding effect and reducing the corrosion current.

The corrosion resistance and protection mechanism are evaluated by EIS. Fig. 5 shows the Nyquist and Bode plots of the three specimens after

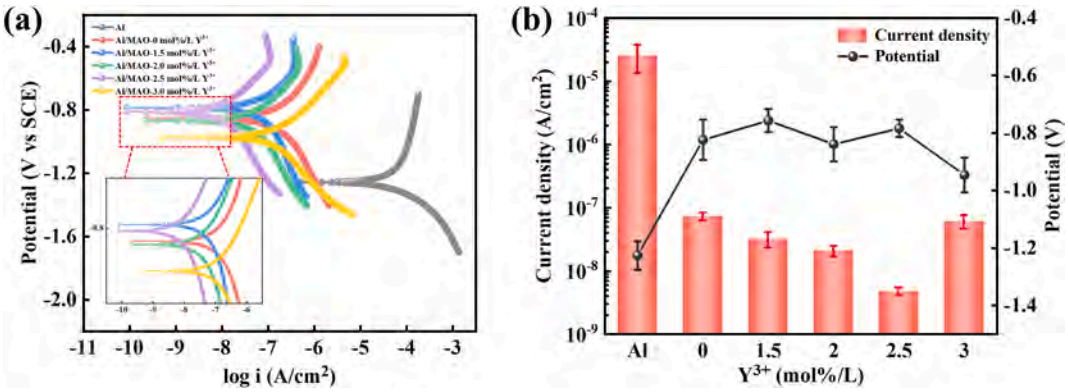

Fig. 4. Electrochemical properties of Al and MAO samples with different Y^{3+} concentrations: (a) Tafel curves and (b) i_{corr} and E_{corr}.

immersion in NaF for 12, 24, 48, and 72 h. The dots represent the experimental data and the solid lines are the fitted data. The capacitance radii of different samples in the Nyquist plots show that the Y-doped coating has the largest capacitance ring radius for the same immersion time. The larger the radius size of the capacitor ring, the stronger the resistance to electron exchange and the lower the electron exchange capacity. In general, the radius of the capacitance ring is related to the corrosion rate, and the Y-doped MAO coatings are more resistant to fluorine corrosion, which is consistent with the Tafel curves. For both the substrate and Al/MAO-0 mol%/L Y^{3+} during initial deterioration, the rapid decrease of the capacitance ring in the high-frequency region indicates that initial corrosion mainly concentrates in the outer layer.

Fig. 5 (a_2-c_2) and (a_3-c_3) show the Bode plots of the three samples. The impedance module |Z| and phase angle (θ) are plotted as a function of frequencies. In the low-frequency region, the module (|Z|) is usually positively correlated with the corrosion resistance of the coating [48]. In general, the impedance of the samples decreases with immersion time, contrary to the aluminum alloy substrate. The impedance of the aluminum alloy in the low-frequency region increases gradually with immersion time from 0 to 72 h due to the surface passivation film. The total impedance of 0 mol%/L Y^{3+} coating is 2.68×10^5 Ω·cm^2 after 12 h, and it is two orders of magnitude larger than that of the aluminum alloy substrate (2.11×10^3 Ω·cm^2). The impedance increases with Y^{3+} doping reaching a maximum of 6.78×10^5 Ω·cm^2. With increasing immersion time, the impedance of the conventional MAO coating decreases rapidly. In particular, the decrease reaches 66.4 % within 12 to 24 h, indicating severe damage by fluoride ions. The 'differential oxygen concentration pool' may form in the MAO coating, where the high fluoride ion concentration, low oxygen content and challenging oxygen diffusion within the pores make it difficult for MAO to provide a favorable internal passivation environment. On the contrary, the Y-doped MAO sample impedance does not decrease. After 48 h, as shown in Fig. 5(a_3-c_3), the phase angle at moderate frequencies becomes higher and wider, indicating that the 2.5 mol%/L Y^{3+} coating is homogeneous and denser. At the same time, the phase angle between the aluminum alloy substrate and the 0 mol%/L Y^{3+} coating decreases rapidly, implying that the coating is penetrated by the electrolyte, and electrochemical reactions occur under the coating [49]. In this stage, 2.5 mol%/L Y^{3+} shows a slower decrease at medium frequencies due to the deposition of corrosion products in the defects. The phase angle arc of 2.5 mol%/L Y^{3+} changes moderately with time constants of less at 48 h and 72 h, suggesting that there is an additional barrier to charge transfer other than the coating as the corrosion-induced formation of surface products hinders charge transfer. The phase angle between the aluminum

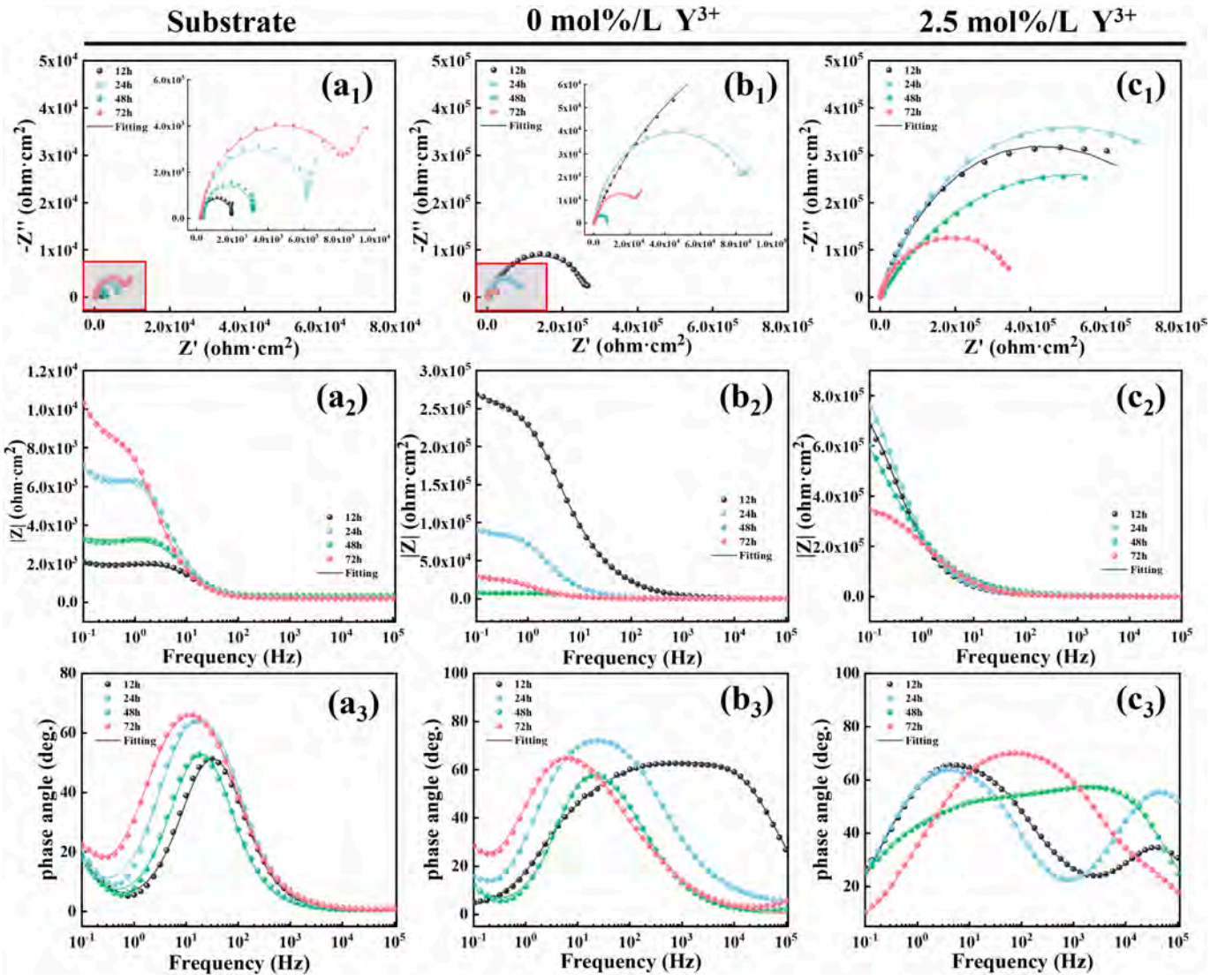

Fig. 5. EIS curves of the 6061 aluminum alloy substrate, Al/MAO-0 mol%/L Y^{3+} and Al/MAO-2.5 mol%/L Y^{3+} after immersion in 0.1 mol/L NaF for 12, 24, 48, and 72 h: **(a_1-c_1)** Nyquist plots; **(a_2-c_2)** Bode modulus; **(a_3-c_3)** Bode phase plots.

substrate and 0 mol%/L Y^{3+} drops below 10° at high frequencies, implying a gradual loss of the protective ability, but that of 2.5 mol%/L Y^{3+} is greater than 20° at high frequencies representing retarded corrosion [50].

The corrosion behavior of the specimens for different immersion time durations is studied by electrochemical impedance spectroscopy. Fig. 6(a-b) shows the equivalent circuits used to fit the EIS results [51], and the fitted results are shown in Table 2. The selection of the equivalent circuit is balanced by the need to fit the results with the lowest error (Order of magnitude less than or equal to 10^{-3}) and minimize the circuit components [52]. The model used in the fitting is one commonly used for MAO coatings of valve metals and their alloys [53–56]. In the equivalent circuit model, R_s is the solution resistance between the working and counter electrodes. In the fitting process, a constant phase element (*CPE*) is used to replace the capacitor because of the non-ideal behavior of the system, *R* is connected in parallel with the corresponding *CPE* [57,58], and n is the *CPE* index, which represents the deviation or roughness of the ideal smooth surface compared to the *CPE* surface and measures the inhomogeneity of the electrode surface. When *n* is equal to 1, *CPE* behaves as an ideal capacitor [59]. Typically, the time constant corresponds to the number of layers in the MAO coating. For the two-step method the prepared coating consists of a dense layer in the first step, a porous layer in the second step and an interfacial layer between the metal and the coating compared to the one-step method. CPE_d and R_d at high frequencies correspond to the capacitance and resistance response of the external void layer in the MAO coating [49]. The mid-frequency CPE_p and R_p are related to the capacitance and resistance of the internal compact layer in the MAO [49,60]. The low-frequency CPE_{dl} and R_{ct} can be used to describe the double-layer capacitance at the electrolyte-metal interface and the resistance to charge transfer during corrosion [61,62].

Owing to the porous and non-homogeneous characteristics of MAO coatings, the electrical resistance and interfacial double layer capacitance can vary between the surface interfaces as a result of the different crystalline phases, grain sizes, surface roughness at the coating/metal interfaces, and it is difficult to build up the charge as in the case of parallel plate capacitors. Heterogeneity at the microscopic or atomic level produces different surface energy scales, which in turn lead to different levels of charge and discharge at the surface interface location during the reaction. The evolution of the equivalent capacitance (C_e) is derived from Eqs. (4)–(5) according to Toorani et al. [63–66]:

$$C_{e-dl} = CPE_{dl}^{1/n}\left(\frac{1}{R_s}+\frac{1}{R_{ct}}\right)^{n-1/n} \tag{4}$$

$$C_{e-p} = CPE_{p}^{1/n}R_{P}^{1-n/n} \tag{5}$$

The C_{e-dl} and C_{e-p} values are shown in Table 3.

Fig. 6(c-d) and Table 3 show the calculated $R_p + R_d$, R_{ct}, equivalent capacitance C_{e-dl}, and C_{e-p} fitted for all the specimens at different times. After 72 h, $R_p + R_d$ of 2.5 mol%/L Y^{3+} changes from 1.245×10^6 to 3.07×10^5 Ω·cm^2, which is clearly higher than those of the aluminum alloy substrate (1.76×10^3 to 9.03×10^3 Ω·cm^2) and 0 mol%/L Y^{3+} (2.85×10^5 to 3.09×10^4 Ω·cm^2). R_{ct} exhibits a similar trend. Similarly, C_{e-dl} of 2.5 mol%/L Y^{3+} changes from 8.36×10^{-8} to 3.26×10^{-4} μF·cm^{-2}, which is lower than those of the aluminum alloy substrate (2.09×10^{-3} to 1.32×10^{-3} μF·cm^{-2}) and 0 mol%/L Y^{3+} (9.03×10^{-6} to 1.20×10^{-3} μF·cm^{-2}). Microcracks or micropores in the coatings allow corrosive substances to permeate to the metal interface. $R_p + R_d$ of 2.5 mol%/L Y^{3+} decreases with immersion time, which indicates that the electrolyte penetrates into the coating through the pores [67]. However, the overall change is not significant, as fluoride ion has smaller effects on the coating. The value of 0 mol%/L Y^{3+} coating decreases and then increases because corrosion products accumulate on the surfaces or in holes, consequently blocking the penetration of corrosive electrolytes. The main damage occurs within 48 h after which the resistance falls off abruptly. The value of the aluminum substrate increases gradually because of the formation of a passivation layer on the surface of the substrate.

After immersion for 72 h, the order of $R_p + R_d$ remains as follows:

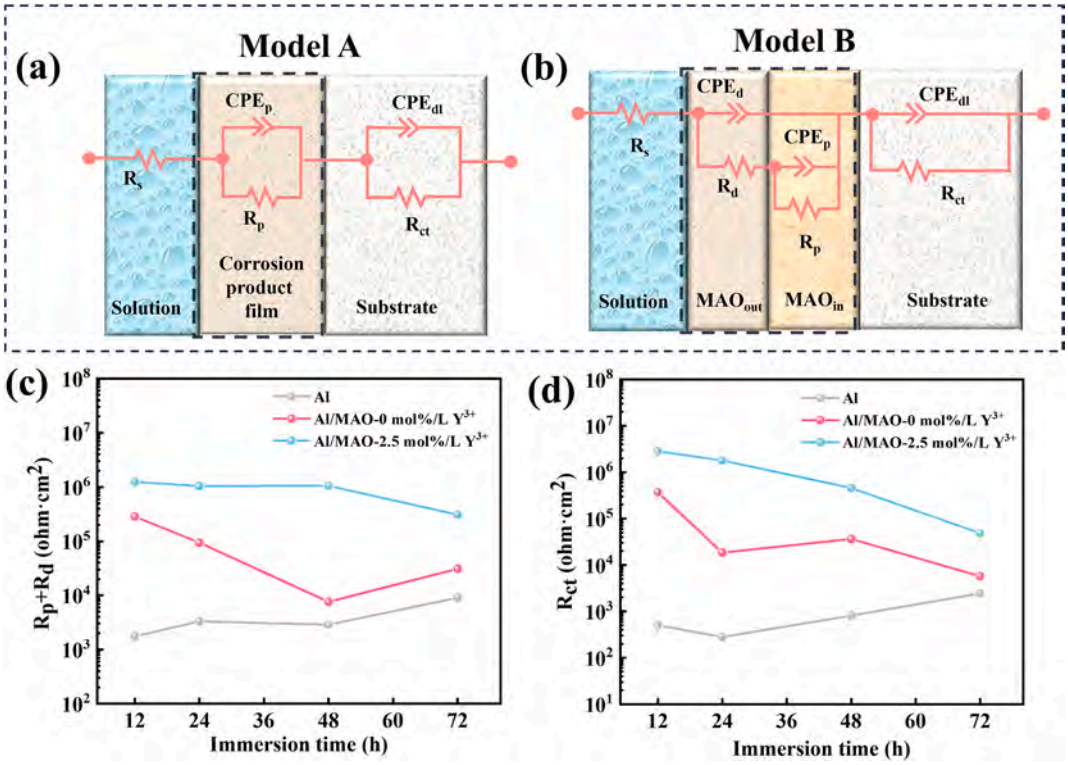

Fig. 6. Circuit model for EIS fitting: (a) Model A for the substrate and (b) Model B for the coating; Variation of fitted parameters in the equivalent circuits: (c) $R_p + R_d$ and (d) R_{ct}.

Table 2
Fitted EIS results of the substrate, Al/MAO-0 mol%/L Y^{3+}, and Al/MAO-2.5 mol%/L Y^{3+} immersed in 0.1 mol/L NaF.

Sample	Immersion times (h)	R_s ($\Omega \cdot cm^2$)	CPE_d ($\Omega^{-1} \cdot s^n \cdot cm^{-2}$)	n_d	R_d ($\Omega \cdot cm^2$)	CPE_p ($\Omega^{-1} \cdot s^n \cdot cm^{-2}$)	n_p	R_p ($\Omega \cdot cm^2$)	CPE_{dl} ($\Omega^{-1} \cdot s^n \cdot cm^{-2}$)	n_{dl}	R_{ct} ($\Omega \cdot cm^2$)	Quality of fit
substrate	12 h	297.4	–	–	–	9.74×10^{-6}	0.972	1.76×10^3	2.37×10^{-3}	0.866	5.05×10^2	6.44×10^{-4}
	24 h	300.6	–	–	–	8.96×10^{-6}	0.956	3.32×10^3	1.94×10^{-3}	0.793	2.81×10^2	1.06×10^{-3}
	48 h	311.4	–	–	–	9.14×10^{-6}	0.988	2.88×10^3	1.68×10^{-3}	0.832	8.12×10^2	8.58×10^{-4}
	72 h	309.1	–	–	–	1.34×10^{-5}	0.921	9.03×10^3	1.64×10^{-3}	0.786	2.45×10^3	3.18×10^{-4}
0 mol%/L Y^{3+}	12 h	305.7	3.66×10^{-8}	0.927	2.34×10^3	4.55×10^{-7}	0.650	2.83×10^5	4.71×10^{-5}	0.722	3.67×10^5	1.27×10^{-4}
	24 h	311.7	5.79×10^{-7}	0.876	3.11×10^2	1.08×10^{-6}	0.884	9.33×10^4	4.41×10^{-4}	0.968	1.85×10^4	3.35×10^{-4}
	48 h	304.5	3.34×10^{-6}	0.918	7.38×10^2	2.13×10^{-6}	0.957	6.87×10^3	1.26×10^{-4}	0.718	3.64×10^4	6.35×10^{-4}
	72 h	330.5	7.58×10^{-6}	0.809	1.13×10^3	1.91×10^{-6}	0.987	2.98×10^4	1.53×10^{-3}	0.762	5.71×10^3	7.03×10^{-3}
2.5 mol%/L Y^{3+}	12 h	314.2	1.97×10^{-7}	0.684	3.47×10^4	1.64×10^{-7}	0.798	1.21×10^6	2.35×10^{-6}	0.684	2.84×10^6	2.77×10^{-4}
	24 h	324.7	4.68×10^{-8}	0.789	6.74×10^3	7.94×10^{-7}	0.709	1.03×10^6	1.54×10^{-5}	0.978	1.79×10^6	3.34×10^{-4}
	48 h	309.2	2.63×10^{-8}	0.947	1.01×10^3	1.22×10^{-6}	0.576	1.05×10^6	8.29×10^{-5}	0.766	4.57×10^5	1.54×10^{-4}
	72 h	307.7	3.26×10^{-8}	0.972	3.39×10^2	5.52×10^{-7}	0.795	3.07×10^5	5.08×10^{-4}	0.807	4.82×10^4	9.05×10^{-5}

Table 3
Calculated C_{e-dl} and C_{e-p} based on EIS fitting.

Sample	Immersion times (h)	$C_{e\text{-}dl}$ ($\mu F \cdot cm^{-2}$)	$C_{e\text{-}p}$ ($\mu F \cdot cm^{-2}$)
substrate	12 h	2.09×10^{-3}	8.67×10^{-6}
	24 h	1.42×10^{-3}	7.62×10^{-6}
	48 h	1.37×10^{-3}	8.75×10^{-6}
	72 h	1.32×10^{-3}	1.12×10^{-5}
0 mol%/L Y^{3+}	12 h	9.03×10^{-6}	1.51×10^{-7}
	24 h	4.11×10^{-4}	7.99×10^{-7}
	48 h	3.51×10^{-5}	1.76×10^{-6}
	72 h	1.20×10^{-3}	1.84×10^{-6}
2.5 mol%/L Y^{3+}	12 h	8.36×10^{-8}	1.09×10^{-7}
	24 h	1.41×10^{-5}	7.32×10^{-7}
	48 h	2.71×10^{-5}	1.47×10^{-6}
	72 h	3.26×10^{-4}	3.49×10^{-7}

2.5 mol%/L Y^{3+} > 0 mol%/L Y^{3+} > substrate, while the trend of C_{e-dl} is the opposite: 2.5 mol%/L Y^{3+} < 0 mol%/L Y^{3+} < substrate. In general, larger capacitance and smaller resistance represent the reduction of the passive layer thickness at the interface and the degradation of the coating [68]. $R_p + R_d$ of 2.5 mol%/L Y^{3+} (3.07×10^5 $\Omega \cdot cm^2$) is almost one order of magnitude larger than that of 0 mol%/L Y^{3+} coating (3.09×10^4 $\Omega \cdot cm^2$). As a result, 2.5 mol%/L Y^{3+} has better corrosion resistance. The structural stability of the coating is important because high porosity tends to be a preferred site for corrosion enhancing scattering effects and forming pitting. The uneven distribution of the coating surface causes the expansion of the electrical differences among different micro-areas, while more cracks increase the likelihood of corrosive fluoride ions destroying the coating. During the corrosion process, fluoride ions tend to preferentially adsorb at micropores and penetrate through irregular discharge channels to the substrate [69]. In conclusion, Y^{3+} doping improves the fluorine corrosion resistance, and 2.5 mol%/L shows the smallest corrosion current density and largest capacitance radius.

3.4. Immersion corrosion

In order to assess the long-term corrosion resistance, the three specimens are submerged in 0.1 mol/L NaF for 3, 7, 18, 24, and 28 days, and the corroded morphology is shown in Fig. 7. After 3 days, the 6061 aluminum substrate loses the metallic luster and corrosion pits appear. Aluminum alloys are passivated by surface oxide under ambient conditions and in aqueous solutions with pH between 4.5 and 8.5. Here, the corrosion rate of the aluminum alloy is limited by its dissolution rate. The addition of sodium fluoride makes the micro anodic reaction change from reaction (6) to reaction (8), and the equilibrium potential of the electrode shifts negatively. On the other hand, fluoride ions destroy the surface oxide to accelerate dissolution [70]:

Micro anode:

$$Al - 3e^- \rightarrow Al^{3+} \tag{6}$$

Micro cathode:

$$H_2O + 2O_2 + 4e^- \rightarrow 4OH^- \tag{7}$$

When F^- is added to the solution, its corresponding anodic reaction becomes:

$$Al + 6F^- - 3e^- \rightarrow AlF_6^{3+} \tag{8}$$

At the same time, the surface morphology of 0 mol%/L Y^{3+} begins to show some traces of corrosion but not corrosion pits. On the other hand, 2.5 mol%/L Y^{3+} coating does not show any changes, implying that Y improves the corrosion resistance. As immersion proceeds, the surface of 0 mol%/L Y^{3+} becomes darker. On the 18th day, partial dissolution at the edge of the coating produces localized scale-like shedding, and it is more severe on the 28th day, with a significant increase in the area and density of shedding exposing the aluminum alloy substrate gradually. However, the corrosion of the coating is significantly suppressed with only minor corrosion observed after Y doping.

3.5. Microstructural evolution of corroded coatings

Fig. 8 shows the surface morphology and EDS spectra of the three specimens after immersion in 0.1 mol/L NaF solution for 28 days. The aluminum substrate is covered by a stacked layer of grainy substance consisting of mainly oxides of F and Al (Fig. 8(a_1-a_3)). For conventional MAO coatings, severe corrosion occurs after 28 days, and some of the coatings rupture due to micro-defects and volume expansion of defects under attack generating large corrosion transition areas by fluoride ions. A large number of cracks on the sample surface due to corrosion of the

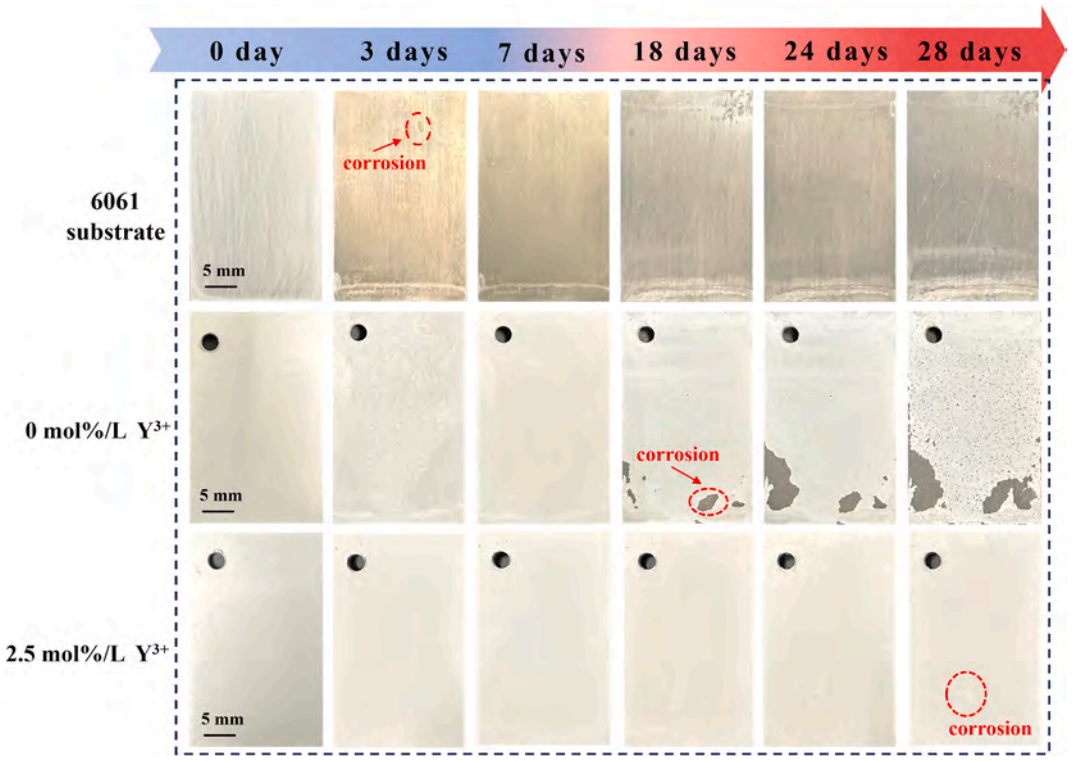

Fig. 7. Macroscopic morphology of the specimens immersed for different times in 0.1 mol/L NaF.

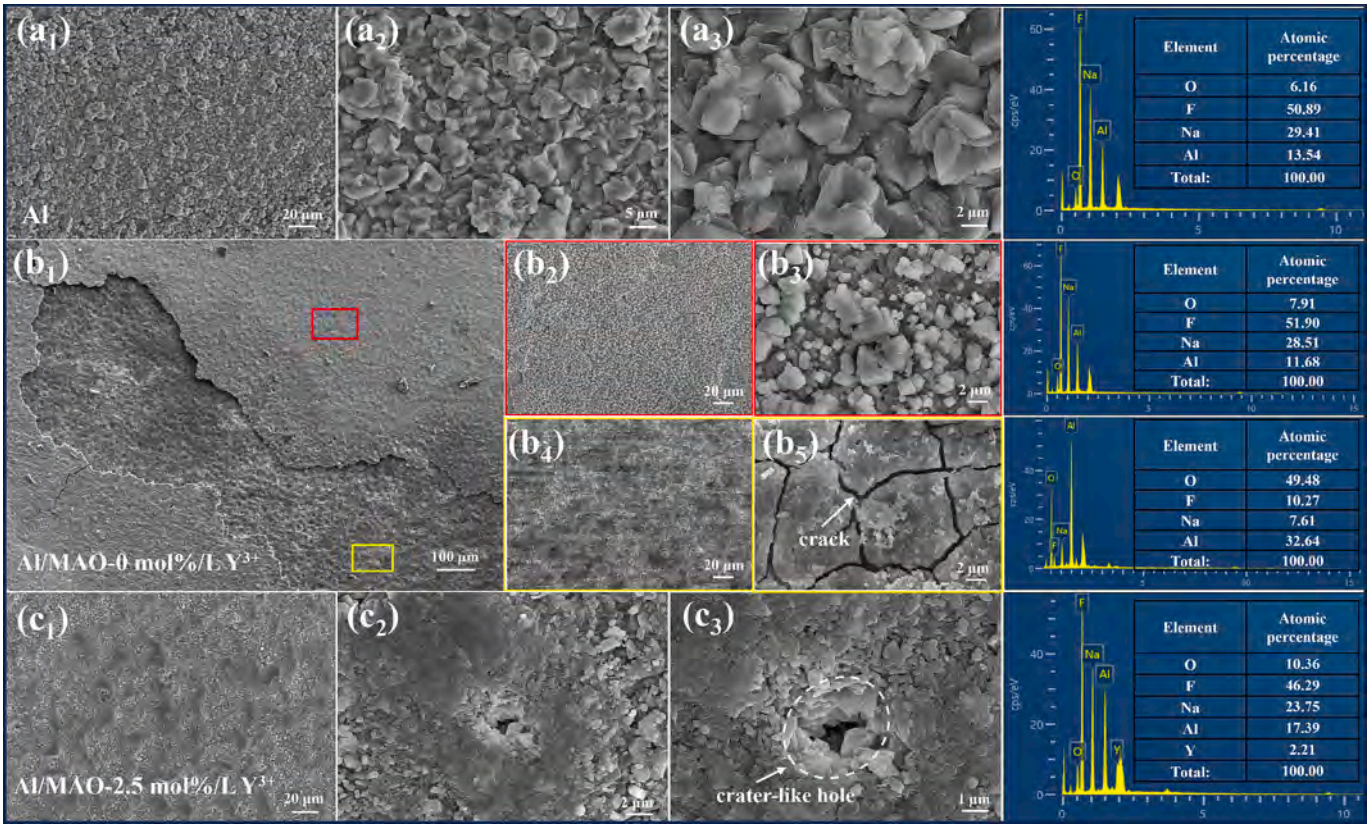

Fig. 8. SEM images and EDS spectra after immersion in 0.1 mol/L NaF solution for 28 days: **(a_1-a_3)** 6061 aluminum alloy, **(b_1-b_5)** Al/MAO-0 mol%/L Y^{3+}, and **(c_1-c_3)** Al/MAO-2.5 mol%/L Y^{3+}.

underlying substrate and incomplete stripping of the outer coating are observed, which not only increases the actual corrosion area of the sample, but results in the presence of high residual stresses, making it an active area prone to corrosion. EDS shows more than 50 % F on 0 mol %/L Y^{3+} reflecting a high degree of F adsorption. The O to Al concentration ratio on the inner surface is 1.52 and larger than that of 2.5 mol %/L Y^{3+} (0.54) indicating a higher degree of oxidation for 0 mol%/L Y^{3+} [71]. The surface of 0 mol%/L Y^{3+} has micro- and nano-corrosion products (Fig. 8(b_1-b_3)) and poor adhesion strength. Warped edges mean that the coating has lost its ability to protect the substrate. In contrast, after 28 days, 2.5 mol%/L Y^{3+} retains the typical crater morphology of micro-arc oxidation. After corrosion, some dense particles cover the surface of 2.5 mol%/L Y^{3+} (Fig. 8(c_2)) and also penetrate into the coating interior (Fig. 8(c_3)), thus reducing the contact area between fluoride ions and the substrate. The Y-doped MAO coating after immersion has a larger Al concentration of 17.39 % than the undoped MAO coating (11.68 %) in addition to a smaller F concentration of 46.29 %, which exhibits lower aluminum oxide corrosion and fluoride absorption behavior. The Y concentration decreases from 5.77 % to 2.21 %, suggesting its positive impact on the corrosion resistance.

The evolution of the microstructure of the corrosion products of the two MAO coatings is observed by TEM. Fig. 9(a, b) show that the

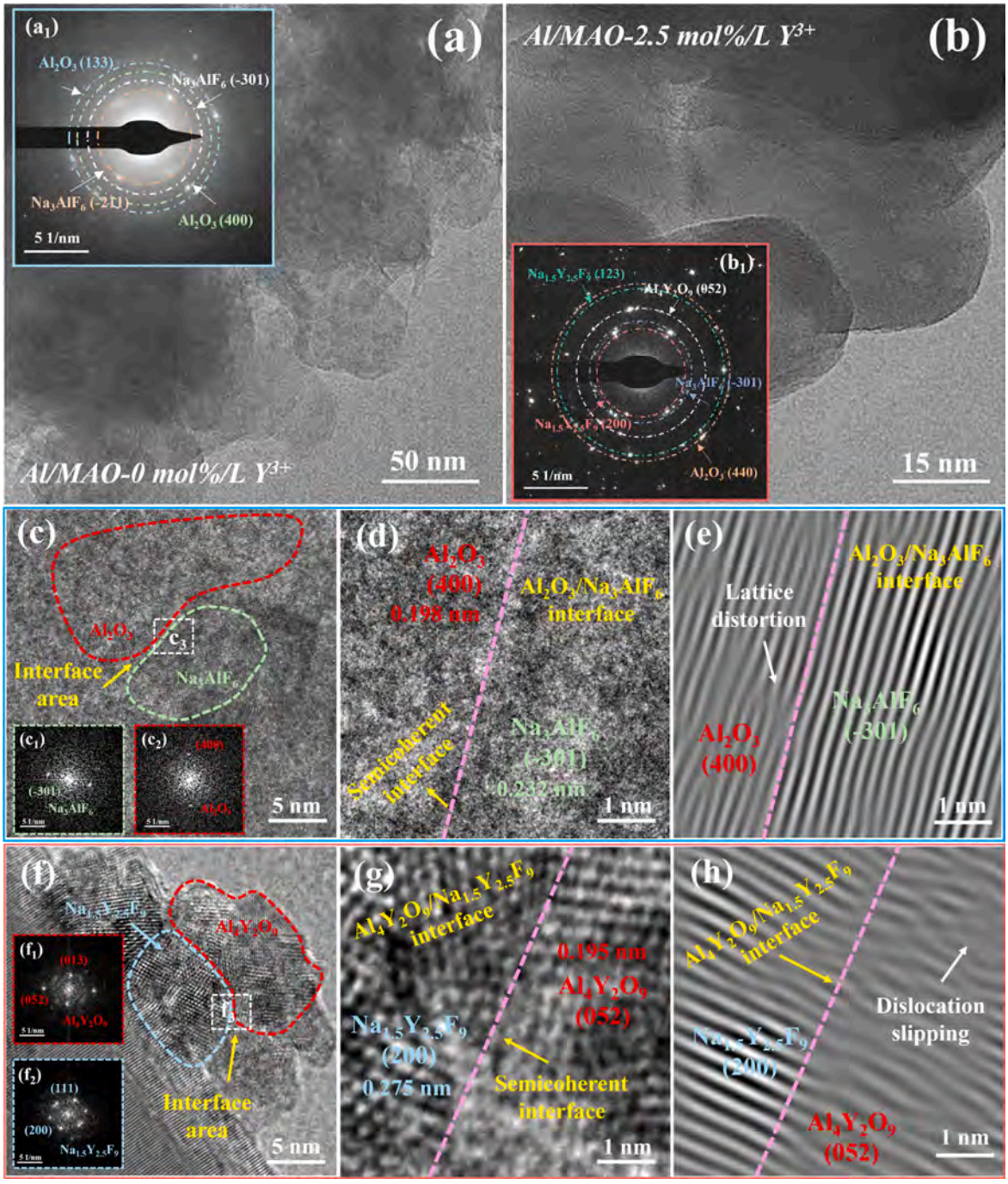

Fig. 9. TEM images of the corrosion products after immersion for 28 days in 0.1 mol/L NaF solution and their SAED images: **(a, a_1)** Al/MAO-0 mol%/L Y^{3+} and **(b, b_1)** Al/MAO-2.5 mol%/L Y^{3+}; **(c)** HR-TEM image of the corrosion product of Al/MAO-0 mol%/L Y^{3+}; **(c_1, c_2)** FFT image of the selected region in (c); **(d)** Zoomed image of the labeled region (c_3) in (c); **(e)** IFFT analysis of (d) images; **(f)** HR-TEM image of the corrosion product of Al/MAO-2.5 mol%/L Y^{3+}; **(f_1, f_2)** FFT image of the selected region in (f); **(g)** Zoomed image of the labeled region (f_3) in (f); **(h)** IFFT analysis of (g) images.

corrosion product on Al/MAO-0 mol%/L Y^{3+} is mainly composed of Al_2O_3 and Na_3AlF_6 (Fig. 9(a_1)), whereas that on Al/MAO-2.5 mol%/L Y^{3+} consists of Al_2O_3, $Al_4Y_2O_9$, Na_3AlF_6, and $Na_{1.5}Y_{2.5}F_9$ (Fig. 9(b_1). These substances are also identified by XRD (Fig. S3). Fig. 9(c_3) shows the interface between Al_2O_3 and Na_3AlF_6 in the corrosion product on Al/MAO-0 mol%/L Y^{3+} revealing orientations of (400) and (−301), respectively. The fast Fourier transform (FFT) images are shown in Fig. 9 (c_1, c_2). Fig. 9(d) shows the magnified region of Fig. 9(c_3), and Fig. 9e shows the inverse fast Fourier transform (IFFT) of Fig. 9d. Fig. 9(f-h) shows the HR-TEM images and fast Fourier transform spectra of the corrosion products on the Y-doped MAO coatings. The lattice distortion at the double interface suggests that (400) Al_2O_3 // (−301) Na_3AlF_6 and (052) $Al_4Y_2O_9$ // (200) $Na_{1.5}Y_{2.5}F_9$ inter-diffuse at the interface (Fig. 9 (e, h)) [72]. Meanwhile, the semi-coherent formation mode at the interface may be related to the periodic fringe dislocation arrays at the interface, and different dislocations affect the interactions at the interface and corrosion [73].

3.6. Wear properties

Fig. 10 shows the wear results of the three samples under a 2 N load and reveals different degrees of wear. The aluminum substrate exhibits wider and deeper indentations, while the cold welding effects on softer aluminum alloy surfaces due to abrasive and adhesive wear, and debris are observed from the wear track [70]. Under dry friction conditions, the wear track on Al/MAO-0 mol%/L Y^{3+} is relatively flat and wide, and exhibited a wider wear track (746.2 μm) after immersion, showing its low resistance to fluoride ion corrosion. Owing to the high hardness and roughness of the ceramic coating, the micro-convex body is damaged in the friction process and it is unable to withstand large shear forces. The MAO coating is corroded heavily by fluoride ions which penetrate through the micropores, and the detached film is unable to provide effective protection leading to more severe wear. On the contrary the substrate shows a narrower and shallower wear track after immersion, showing a lower wear rate and smoother friction surface.

According to calculations, Young's modulus of the Y-doped MAO

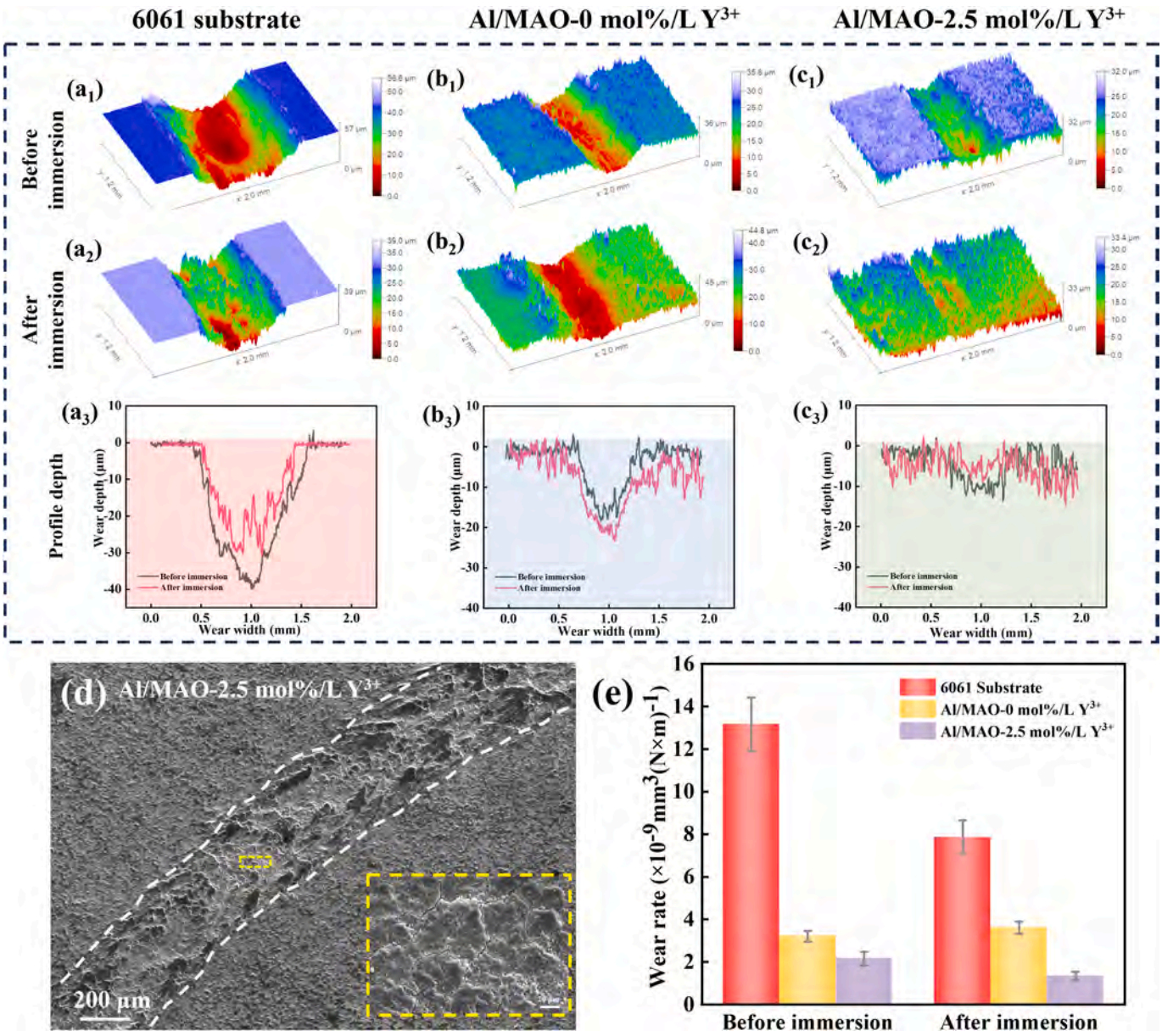

Fig. 10. 3D morphology and line scans after wear: **(a_1- a_3)** 6061 aluminum alloy substrate; **(b_1- b_3)** Al/MAO-0 mol%/L Y^{3+}; **(c_1- c_3)** Al/MAO-2.5 mol%/L Y^{3+}; **(d)** Wear morphology of the Y-doped MAO coating after immersion and local area enlargement; **(e)** Wear rates before and after immersion.

coatings decreases from 411 Gpa to 325 Gpa in the X-direction and from 398 Gpa to 332 Gpa in the Y-direction (Fig. S4), which may be related to the changes in the electronic structure of the aluminum oxides after the Y-doping. This means that under the same load, the Y-doped coatings produce a larger actual contact area in both the X and Y directions to disperse stress. The Y-doped MAO coatings show wider wear tracks and smaller wear depths, which are consistent with the smaller Young's modulus, and the shear stress concentrates at the edge. After immersion in 0.1 mol/L NaF, the coating retains the high wear resistance. Fig. 10d shows some cracks and wear debris, and the smaller wear rate may be associated with the high-density and high-hardness α-Al_2O_3 phase in the coating [74]. Meanwhile, the surface defects are filled with corrosion particles to reduce the radial cutting and squeezing effects of wear so the wear area decreases [75].

Fig. 11 presents the SEM image and EDS maps of the wear track on the Y-doped MAO coating after immersion. O, F, Al, Si, Na, and Y are identified and the O and Al concentrations increase after wear (Fig. 11i, h), which is associated with the transfer and destruction of the alumina friction balls and coating surface. At the same time, the F, Na, and Y concentrations decrease but that of Si does not change significantly, suggesting loss of Y and that the corrosion product of Y, F, and Na is involved in the wear process.

4. Corrosion mechanisms

4.1. Corrosion mechanisms and growth of MAO coatings

Fluorine corrosion of aluminum alloys depends on the chemical composition, microstructure, phase, and morphology. The three key components involved in the MAO process are the aluminum substrate, the MAO coating, and the electrolyte. The growth of MAO coatings is associated with the formation and dissolution of redox reactions under an electric field at interface 1 between the 6061 aluminum substrate and MAO layer and interface 2 between the MAO layer and electrolyte [76,77]. The growth and chemistry of the coating can be analyzed under two processes, which separately operate at interface 1 and interface 2. The reactions at interface 1 are related to cations from the substrate as well as anions from the coating. Compounds and new anionic vacancies are formed during the micro-arc oxidation by the continuous depletion of anions and cations. As the reaction continues, anions from the coating are depleted and anions are supplied by the electrolyte to interface 2 under the action of the electric field for maintaining the equilibrium in the reaction [78]. With the continuous replenishment of anionic vacancies (primarily oxygen ionic vacancies), new anions continue to be imported into the substrate at interface 1. This process repeats itself until the end. However, the discharge cascade results in the growing coating that prevents the substrate and electrolyte from coming into contact with each other. In fact, the reaction at interface 1 takes place in an oxygen-deficient atmosphere. Under these conditions, the conditions for the formation of stoichiometric aluminum oxide cannot be met [79]. The reaction occurring at interface 1 is shown below [80]:

$$Al_M \rightarrow Al_{Al_2O_3} + 3/2V_{\ddot{O}} + 3e^- \quad (9)$$

The aluminum atom Al_M located in the conventional sites of the valve metal substrate in the anoxic environment are converted into $Al_{Al_2O_3}$ sites on the formed ceramic coating under the action of an electric field and oxygen vacancies are formed. According to the point defect model (PDM), the oxygen vacancies or cation gaps are electron donors and the sample has n-type semiconducting characteristics.

As for interface 2, the reactions occur partially at the electrolyte and MAO coating as shown below [81]:

$$V_{\ddot{O}} + H_2O \rightarrow O_{Al_2O_3} + 2H^+_{aq} \quad (10)$$

$$V_{\ddot{O}} + OH^- \rightarrow O_{Al_2O_3} + H^+_{aq} \quad (11)$$

Reactions (10) and (11) indicate that H_2O and OH^- during oxidation form oxide film conventional sites O replenish oxygen vacancies created during reaction (9) by separating H^+_{aq} into the electrolyte. The other half of the reaction at interface 2 involves the reaction of Al^{3+} with the anions XO_y^{Z-} (PO_4^{3-}, SiO_3^{2-}) in the electrolyte, and also in the plasma cluster excited states of oxygen from these anions will be formed to combine with Al^{3+} and oxygen vacancies. The XO_y^{Z-} anions bind with Al^{3+} to form new compounds, which play an essential role in promoting oxidation as shown below [78,82]:

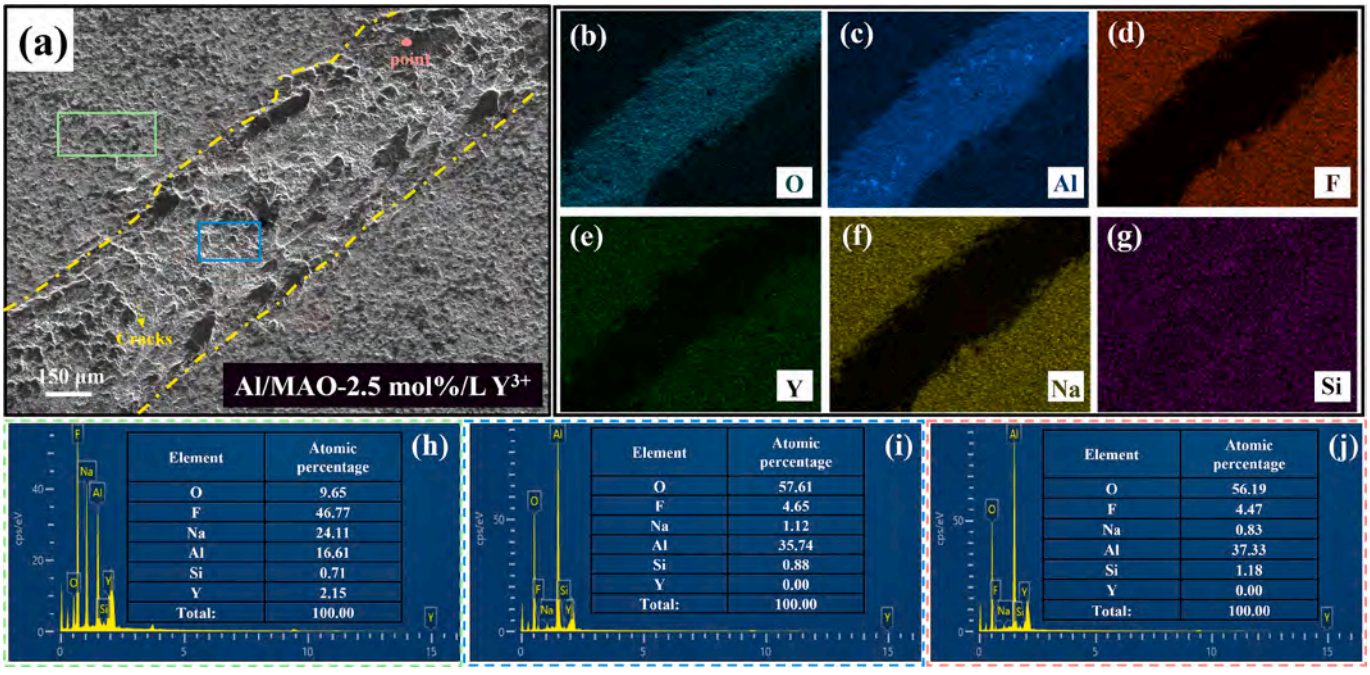

Fig. 11. Wear images and elemental distribution of Y-doped MAO coatings after immersion: **(a)** Wear track morphology; **(b)** O; **(c)** Al; **(d)** F; **(e)** Y; **(f)** Na; **(g)** Si; **(h)** Elemental composition of the green box in (a); **(i)** Elemental composition of the blue box in (a); **(j)** Elemental composition of the red dot in (a).

$$(NaPO_3)_6 + 6H_2O \rightarrow 6NaH_2PO_4 \quad (12)$$

$$NaH_2PO_4 \rightarrow PO_4^{3-} + 2H^+ + Na^+ \quad (13)$$

$$PO_4^{3-} + Al^{3+} \rightarrow AlPO_4 \quad (14)$$

$$2SiO_3^{2-} + 6Al^{3+} + 7O^{2-} \rightarrow Al_6Si_2O_{13} \quad (15)$$

From reactions (12)–(15), it can be observed that a large amount of Al^{3+} is consumed. This also produces a flow of Al^{3+} from the substrate to the coating to react with anions in the electrolyte, reducing the requirement of oxygen ions and suppressing the production of oxygen vacancies in reaction (9). Overall, Al^{3+} in the coating moves constantly to interface 2, while oxygen ions move in the opposite direction to interface 1. These repetitive reactions promote the continuous growth of the MAO coating. The addition of yttrium nitrate increases the concentration of anions and the conductivity of the electrolyte (Fig. 1(b)), which contributes to the rate of electron and ion transport migration and enhance the rate to react between the anionic groups XO_y^{Z-} and Al^{3+} in electrolyte [83]. This leads to a deficit in the anionic reaction with Al^{3+}. In order not to affect the reaction at interface 1, XO_y^{Z-} tends to achieve equilibrium by taking Al^{3+} from the substrate. Anionic group combines with Al^{3+} in the substrate and reaction (9) is inhibited to reduce the production of oxygen vacancies [84].

4.2. Corrosion mechanisms, modulated coating structure, and adsorption of corrosive medium

The wide bandgap φ_0 renders the MAO coating electrically insulating. During MAO, electrons are injected into the conduction band of the metal oxide coating in two ways: (1) Oxidation/reduction (O/R), which overcomes the solid–liquid barrier by tunneling and enters the conduction band to generate the initial current, and (2) Incorporation of dopants which form energy levels in the forbidden band enabling electrons to move to the conduction band to generate a current. The effects of the changes in the energy bands are studied by determining the DOS and oxygen vacancy formation energy before and after the incorporation

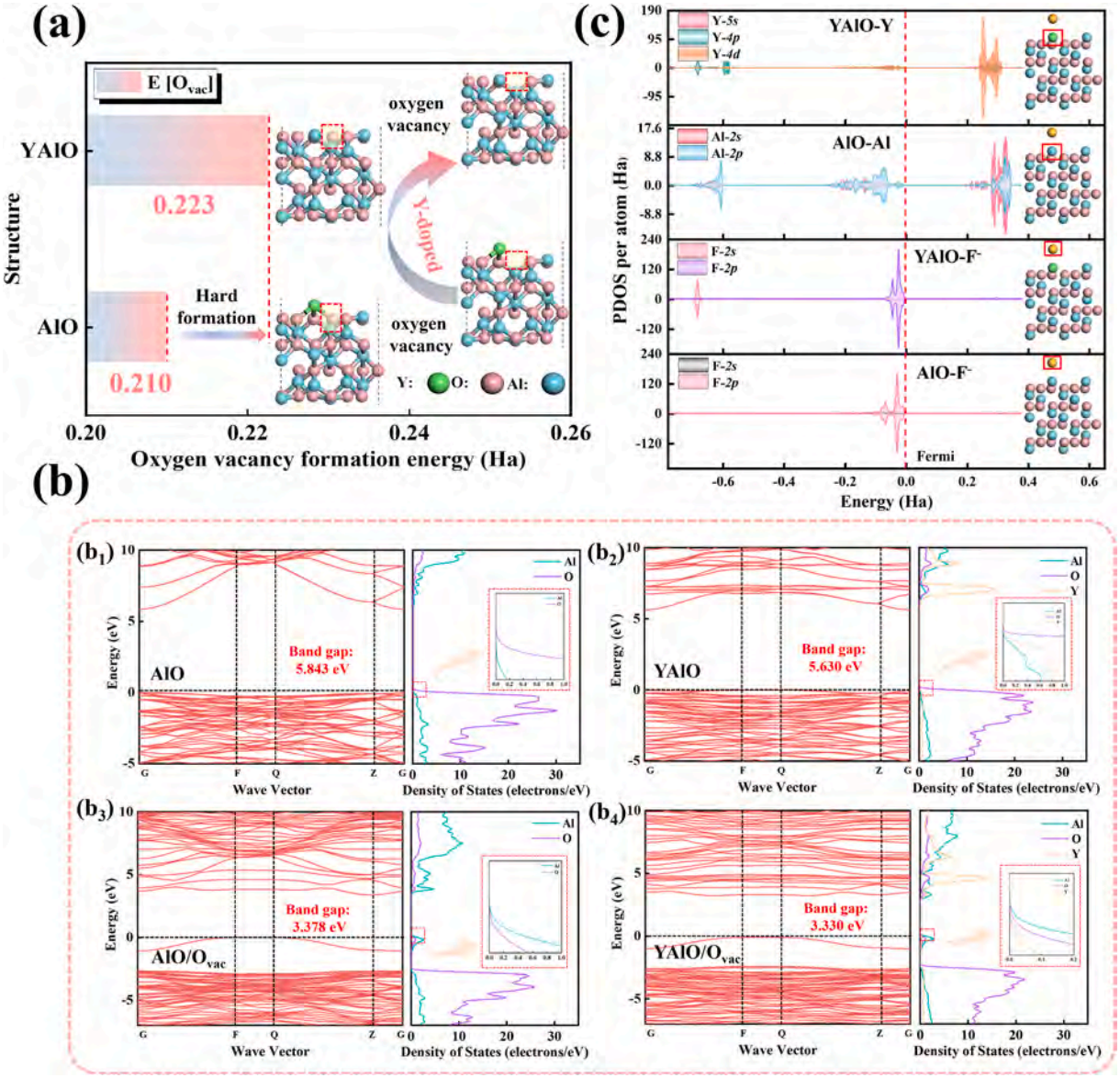

Fig. 12. (a) DFT calculations of oxygen vacancy formation energies of MAO coatings with and without Y-doping (Structural model shown in the insert); Band structure and DOSs with and without Y-doped MAO coatings: **(b_1, b_2)** AlO, YAlO; **(b_3, b_4)** AlO/O_{vac}, $YAlO/O_{vac}$; **(c)** PDOS of Y, Al and F^- orbitals in AlO and YAlO coatings in the presence of F adsorption (The structural model and the corresponding elaborated atoms (in red boxes) are shown in the insertion).

of Y, as shown in Fig. 12ab. Fig. 12b shows Y substitution reduces the bandgap from 5.843 eV (that of pure alumina is 5.85 eV [85]) to 5.630 eV. In the presence of oxygen vacancies and Y atoms, the bandgap of aluminum oxide decreases from 3.378 eV to 3.330 eV. The results show that the YAlO coating has a lower bandgap width. YAlO insulating coatings with lower bandgap widths have higher electron mobility compared to AlO coatings, which allows electrons to escape more easily and charges to take more paths through the coating for breakdown to occur [86,87]. This facilitates the formation of multiple discharge points and avoids the concentration of the electric field in certain weak areas, resulting in relatively uniform breakdown discharges. Therefore, regulating proper coating conductivity is crucial to obtaining dense, uniform, and corrosion-resistant coatings. In addition, alumina contains oxygen vacancies which affect the conductivity. An excessively high electrical conductivity affects the nucleation and growth rates during MAO and reduces the impedance between the electrodes (electrolyte and substrate) that form the electric field, thereby making it more difficult for the plasma discharge to form. Moreover, oxygen vacancies provide more adsorption sites for anions and accelerate F-induced corrosion. According to the point defect model, passivation film growth depends on the formation and diffusion of cation/anion vacancies [88]. By reducing the number of anionic vacancies, the mobility of cationic vacancies and pitting can be reduced. Fig. 12a shows that Y increases the oxygen dissociation energy (oxygen vacancy formation energy) of alumina from 0.210 Ha to 0.223 Ha. It is more difficult to form oxygen vacancies in the YAlO coatings at the same energy and Y inhibits the generation of oxygen vacancies and reduces leakage during the discharge. As a result, the electric field increases to make the discharge more stable reducing the extent of defects in the coating [84]. All in all, our calculations reveal that Y not only regulates the electrical conductivity, but also promotes the formation of corrosion-resistant structures in the oxide coating since vacancies are prone to adsorption of fluoride ions.

The above findings are important for understanding the fluorine corrosion resistance of coatings. The corrosion process in the fluoride environment is described in the following. Corrosion occurs because small radius F^- enters the aluminum oxide ceramic coating to produce a strong inductive ionic conductivity, making the coating in some specific points of the occurrence of the ionic chaotic movement. When the electric field at the coating/solution interface reaches a critical value, pitting and dissolution occur as shown in the following [89]:

$$Al \rightarrow Al^{3+} + 3e^- \tag{16}$$

In the sodium fluoride medium, the following reactions occur on the cathode [90]:

$$O_2 + 2H_2O + 4e^- \rightarrow 4OH^- \tag{17}$$

$$Al^{3+} + 3OH^- \rightarrow Al(OH)_3 \tag{18}$$

$$(Al_2O_3)_n Al_2O_3 + 3H_2O \rightarrow (Al_2O_3)_n \left(Al(OH)_3\right)_2 \tag{19}$$

At the micropores and cracks, F^- accumulates and adsorbs onto the coating surface to displace hydroxyl groups of aluminum hydroxide until equilibrium [91–93]:

$$(Al_2O_3)_n \left(Al(OH)_3\right) + F^- \rightarrow (Al_2O_3)_n Al(OH)_2F + OH^- \tag{20}$$

$$(Al_2O_3)_n Al(OH)_2F + F^- \rightarrow (Al_2O_3)_n Al(OH)F_2 + OH^- \tag{21}$$

In the early stage of corrosion, F^- adsorbs onto the surface *via* pores and defects, followed by coalescence of isolated pores to form larger pores. When enough corrosion products accumulate on the coating, the passivation film becomes thicker and covers the initial pores. As the pores are sealed, oxygen cannot enter. Therefore, the internal F^- concentration does not decrease, leading to increased internal corrosion. At the same time, the external ceramic coating will continue to dissolve leading to ultimate destruction. It is important to note that fluoride ions have a smaller ionic radius than several other halogen elements (e.g. Cl^-, Br^-, and I^-) due to their smaller shielding effect and lower inter-electron repulsion. Based on this, fluoride ions are highly permeable to penetrate highly defective coatings, causing them to accumulate in micro-defects and cracks, leading to increased localized corrosion. Therefore, Y-doped MAO coatings with low defects and fewer pores show better resistance to fluorine corrosion by reducing the penetration path of fluoride ions in small radii and lowering the chance of direct contact with the substrate.

According to the law of matching affinities, during fluoride corrosion of MAO coatings, well-hydrated kosmotropes fluoride ions are more inclined to adsorb on the surface of the coating and interact with Al^{3+} to form the corresponding fluorine complexes during the fluorine corrosion of MAO coatings (since all metal cations with valence greater than 1 belong to kosmotropes [8]). It is necessary to investigate the adsorption relationship between fluoride ions and coatings, which is essential for understanding the corrosion resistance of coatings to kosmotropes fluoride ions. The interactions between fluorine and aluminum oxide in the solution are analyzed by an adsorption model. As shown in Fig. 13a, the adsorption energy of pure aluminum oxide increases from −0.1822 Ha to −0.1613 Ha after the introduction of Y. The binding distance between F^- and surface atoms increases from 1.734 Å to 2.166 Å, making adsorption less [94]. Since F^- in a solution undergoes Brownian motion, desorption occurs, and less adsorption improves the corrosion resistance. This is confirmed by the smaller F concentration in Fig. 8. Fig. 12c shows the partial density of states (PDOS) of AlO and YAlO, which helps to understand the electronic structures [85]. The change in electron transfer stems from the interactions between the Al 2 *s* and Al 2*p* orbitals with F 2*p* orbitals. In the substitution model, the interactions between Y 4*p* and Y 4*d* orbitals with F 2 *s* and F 2*p* orbitals may be responsible for the weaken adsorption. In addition, the difference in the degree of overlap of the Al 2*p* and F 2*p* orbitals in the two models may be attributed to the change in the type of adsorption, which affects the adsorption effect on F^-, and consequently alters the fluorine corrosion resistance of the coatings.

The structures of YAlO and AlO are compared. The bond lengths of O_2-Al_3 and O_2-Al_4 and charge transfer of Y_1 and O_2 atoms are presented in Fig. 13(b-d), respectively (refer to Fig. S5 of the Supporting Material for the precise location of the atomic layer symbols), to study the change of covalent bond strengths [95]. After Y incorporation, the average bond length of O_2-Al_3 decreases from 1.799 Å to 1.787 Å and that of O_2-Al_4 diminishes from 1.893 Å to 1.879 Å (Fig. 13c). At the substitution sites, the charge transfer values of Y_1 and Al_1 are 1.438|e| and 1.271|e|, respectively, which are mainly determined by the electronic structures. Y substitution increases the charge transfer of Al_1 from 1.097|e| to 1.114|e|, and the average charge transfer of the adjacent-row O_2 from −0.864|e| to −0.878|e| (Fig. 13d). The increased charge transfer indicates stronger covalent bonding and chemical stability. Since the bond strength is inversely related to the bond length, the Al-O bond energy in the Y-doped MAO coatings is greater than that of Al-O in MAO coatings. Overall, Y-doped MAO forms a denser and stronger Al-O covalent network, which reduces the penetration of corrosive media and maintains its excellent corrosion resistance under fluoride ion attack.

4.3. Corrosion mechanisms and products

During the fluoride solution immersion process, a protective corrosion product reaction film gradually develops on the coating surface as the corrosion time increases. The formation of reaction film is related to the nucleation and growth process of fluorinated corrosion products [96]. At the same time, defects such as grain boundaries and dislocations act as nucleation sites for particles, and high corrosion dissolution rates promote particle growth [97]. Fluorine is the most electronegative element (Pauling scale), and its atoms are extremely electron-attractive, resulting in the formation of strong ionic bonds that confer a high degree of stability to the crystal structure [9]. However, the lack of overlapping

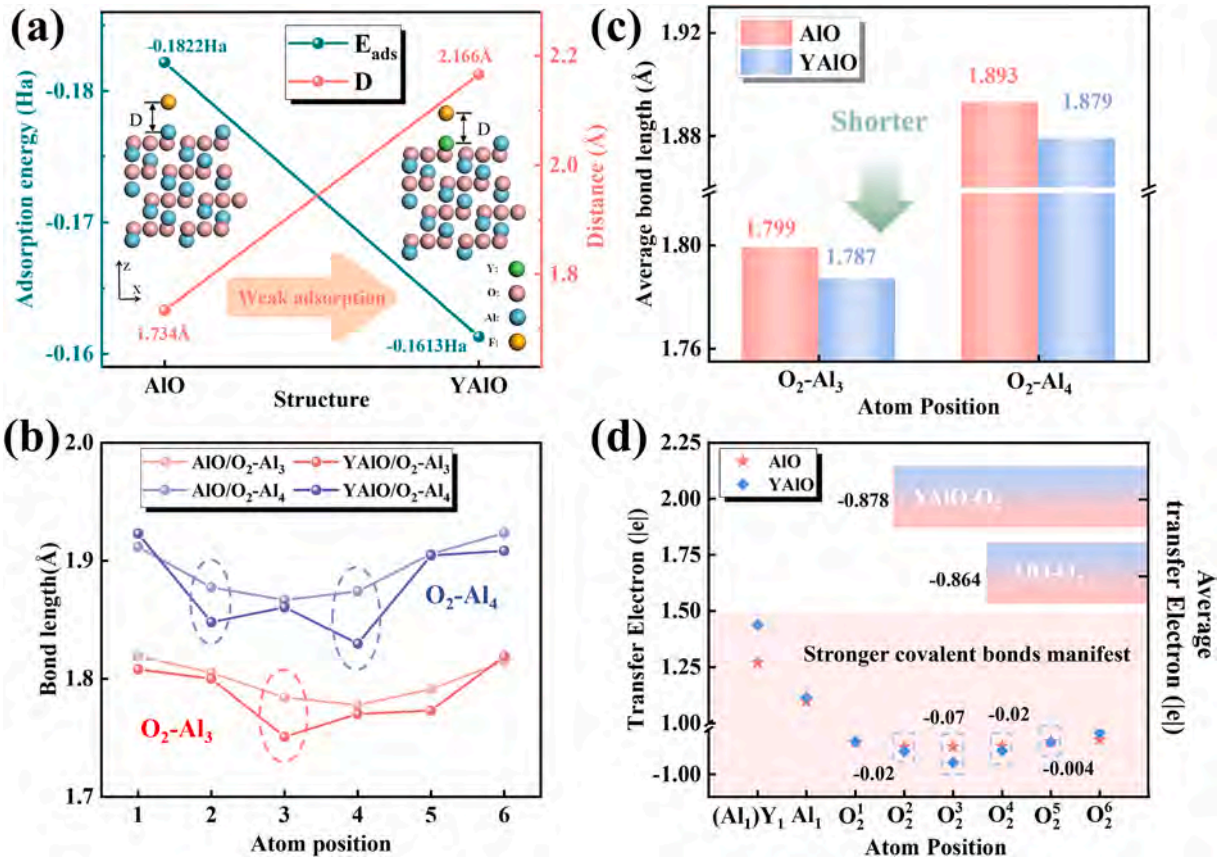

Fig. 13. (a) DFT calculations of the adsorption energy of F^- on MAO coatings with and without Y (Side view of the adsorption structure model shown in the inset); (b) Changes of bond lengths at different atom positions of Al-O bonds in Al_2O_3 coatings with and without Y; (c) Changes in average bond lengths of Al-O bonds in Al_2O_3 coatings with and without Y; (d) Transfer charges at different atom positions in Al_2O_3 coatings with and without Y as well as the average transfer charge from the O adjacent rows of atoms. The atom type symbol X_p^n represents the element (X = Al, O, Y), the number of surface layers (p = 1, 2, 3, 4), and the positions of the atoms in the region (n = 1, 2, 3, 4, 5, 6). (Refer to Fig. S5 in Supporting Material for the precise location of the atomic layer symbols).

electron clouds in metallic or covalent bonds results in a material that lacks ductility and toughness and exhibits significant brittleness. The high electronegativity brings about strong electrostatic interactions in the crystal structure, making it more susceptible to fracture along specific crystal faces. In addition, the strong complexing tendency of fluoride ions in solution exhibits a strong attraction to other ions and molecules, exacerbating the coating dissolution process [8]. The low fracture toughness of fluoride-reactive films makes them more susceptible to defects at high growth rates.

Anyway, the interfacial characteristics between fluorinated corrosion products are investigated to further study the fluorine corrosion resistance of the coatings, as shown in Fig. 9(c-h). The degree of mismatch (δ) is used to evaluate the degree of coherence at the interface between the corrosion product and oxide as shown by Eq. (22) [73]:

$$\delta = \frac{2(d_\beta - d_\partial)}{d_\beta + d_\partial} \tag{22}$$

where δ is the relative difference between the spacings of the atoms of the two neighboring phases at the interface and d_∂ and d_β are the lattice spacings of the two phases. The lattice mismatches at the Al_2O_3/Na_3AlF_6 and $Al_4Y_2O_9/Na_{1.5}Y_{2.5}F_9$ interfaces are calculated to be 0.158 and 0.34, respectively, indicating semi-coherent interfaces. The distance D between each pair of dislocations is derived by Eq. (23) [72,98,99]:

$$D = \frac{(d_\beta + d_\partial)^2}{4(d_\beta - d_\partial)} \tag{23}$$

The dislocation distances at the Al_2O_3/Na_3AlF_6 and $Al_4Y_2O_9/Na_{1.5}Y_{2.5}F_9$ interfaces are 1.36 and 0.69, respectively, showing that lattice distortion and edge dislocation entanglement are more severe at the $Al_4Y_2O_9/Na_{1.5}Y_{2.5}F_9$ interface compared to the Al_2O_3/Na_3AlF_6 interface (Fig. 9c-d). A larger degree of mismatch corresponds to a larger elastic strain energy, which can buffer the tearing of quasi-granular boundaries in Y-doped MAO coatings along the grain direction and generate dislocation slipping [100–102]. Elastic point strain is released as edge dislocations, and suitable dislocation slip facilitates coordinated deformation of the interface and inhibits the growth of microcracks at quasi-crystal boundaries [73]. Multiple slips facilitate lattice-coordinated distortion, mitigate interfacial cracking, and increase the stability of $Al_4Y_2O_9/Na_{1.5}Y_{2.5}F_9$ [103]. After the incorporation of Y, the number of interfacial dislocations increases, and the dislocations are pinned at the interface. The stability of the interface can be improved by regulating the edge dislocations at the interface between the fluorinated corrosion products and the oxide semi-coherent interface. Continuous dislocation pinning mitigates the embrittlement of ionic crystals, inhibits the extension of fluoride cracks, and improves the fluorine corrosion resistance of the coating [12].

4.4. Fluorine corrosion protection mechanism

In Fig. 14 schematic showing the corrosion process is used to illustrate the protection mechanism of the Y-doped assisted MAO coatings. The highly permeable corrosive fluorine solution penetrates easily and longitudinally through the micropores of the outer layer of MAO. The corrosion reaction occurs to produce initial localized damage leading to a larger pH and a gradual increase in the specific surface area, which

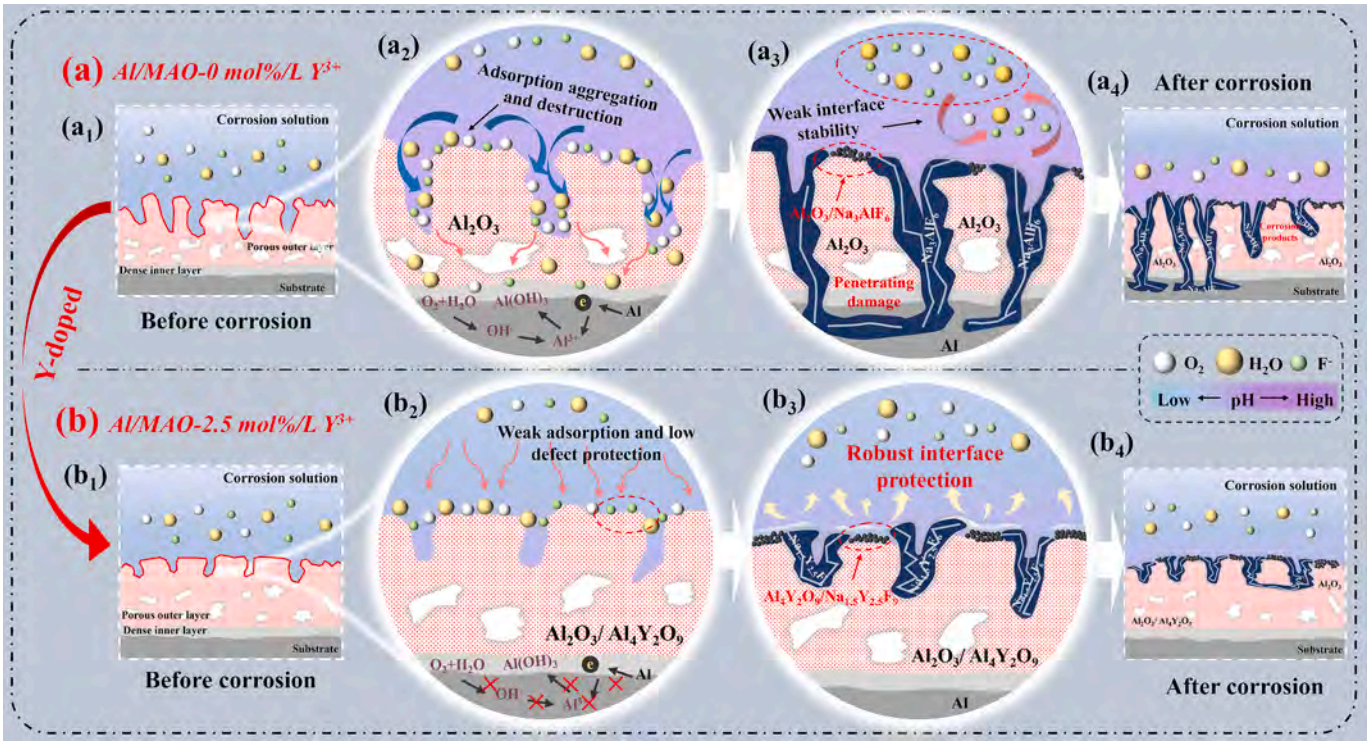

Fig. 14. Schematic diagram of the corrosion mechanism: (a) Al/MAO-0 mol%/L Y^{3+}; and (b) Al/MAO-2.5 mol%/L Y^{3+}.

ultimately reaches the interface between the substrate and the coating to produce large areas of pitting and cracking (Fig. 14a). Before corrosion commences, Y reduces the porosity and increases the density of the MAO coatings to better block the corrosion medium. The impedance of the coating comes mainly from the well-sealed ceramic layer. Furthermore, Y decreases the binding stability of kosmotropes fluoride ions on the surface of MAO coatings, making them easier to desorb from the surface (Fig. 14(b_2)). Y compacts the aluminum-oxygen bond form a denser and stronger Al-O covalent network to mitigate corrosion damage. In addition, Y improves the edge dislocations at the interface between the corrosion product and oxide semi-coherent interface after corrosion has occurred and form chemically stable enhanced $Al_4Y_2O_9/Na_{1.5}Y_{2.5}F_9$ structure corrosion interface, resulting in mitigated crack expansion and corrosion damage in low fracture toughness fluoride reactive films.

5. Conclusions

In this work, an in-situ growth of yttrium assisted affinity fluorine corrosion resistant coating based on two-step micro-arc oxidation was successfully developed on aluminum alloy surfaces. Potentiodynamic polarization test shows that the coating system has corrosion current density of 4.49×10^{-9} A/cm^2 in 0.1 mol/L NaF solution, which is four orders of magnitude lower than the bare substrate aluminum alloy along with a more positive corrosion potential. Experiments and DFT calculations reveal the kinetics of coating growth and the reaction mechanisms at the contact interface synergistically to understand the origin of highly durable fluorine corrosion. DFT calculations demonstrate that yttrium assists in reducing the number of oxygen vacancies and band gap width of the coating, achieving low surface porosity defects and the growth of a strong and robust Al-O covalent network. The dense coating system provides more durable corrosion barriers to small radius and highly permeable fluoride ions, and is capable of being immersed in 0.1 mol/L NaF solution for more than 28 days with little to no corrosion damage. In addition, yttrium doping can reduce the adsorption reaction effect of kosmotropes fluoride ions on the coating surface sufficiently to decrease the depolarization effect. Yttrium in the coating exists as the phase component of $Al_4Y_2O_9$ and forms more stable and effective fluoride corrosion interfacial protective film after corrosion occurs, which is used to mitigate interfacial cracking caused from strong ionic bonding by modulating continuous dislocations pinned to inhibit further corrosion deterioration extension of the coating. The excellent fluorine corrosion protection of yttrium-doped assisted MAO coatings stems from the synergistic effect of the multiple mechanisms described above. The high endurance fluorine corrosion protection also gives the coatings outstanding wear resistance characteristics for performance in corrosive environments. Overall, this work is expected to advance the development of anti-corrosion coating systems for aluminum alloys in highly durable fluorine environments.

CRediT authorship contribution statement

Zishuo Ye: Writing – review & editing, Writing – original draft, Validation, Project administration, Data curation, Conceptualization. **Shu Xiao:** Writing – review & editing, Writing – original draft, Resources, Project administration, Funding acquisition, Conceptualization. **Yinong Chen:** Writing – original draft, Validation, Investigation, Formal analysis, Data curation, Conceptualization. **Shuyu Fan:** Validation, Methodology, Investigation, Data curation. **Yi Wu:** Validation, Methodology, Investigation. **Fenghua Su:** Supervision, Resources, Methodology. **Paul K. Chu:** Supervision, Resources, Project administration.

Declaration of competing interest

The authors declare that they have no known competing financial interests or personal relationships that could have appeared to influence the work reported in this paper.

Acknowledgments

This work was supported by the National Natural Science Foundation of China (Nos. 52375182 and 52005187), Natural Science Foundation of Guangdong Province (No. 2023A1515012308), Fundamental Research

Funds for the Central Universities (No. 2023ZYGXZR030), Basic and Applied Basic Research Foundation of Guangzhou (No. 2024A04J3821), Basic and Applied Basic Research Fund of Guangdong Province (No. 2023A1515240006), and City University of Hong Kong Donation Research Grants (Nos. 9220061 and DON-RMG No. 9229021).

Data availability

Data will be made available on request.

References

[1] D. Kumar, S. Singh, S. Angra, Dry sliding wear and microstructural behavior of stir-cast Al6061-based composite reinforced with cerium oxide and graphene nanoplatelets, Wear 516 (2023).
[2] R. Kreethi, Y.-J. Hwang, H.-Y. Lee, J.-H. Park, K.-A. Lee, Stability and plasma etching behavior of yttrium-based coatings by air plasma spray process, Surf. Coat. Technol. 454 (2023).
[3] S. Fan, S. Xiao, S. Lin, F. Su, Y. Su, P.K. Chu, Macroscale superlubricity and durability of in situ grown hydrogenated graphene coatings, Chem. Eng. J. 459 (2023).
[4] S. Fan, Y. Chen, S. Xiao, K. Shi, X. Meng, S. Lin, F. Su, Y. Su, P.K. Chu, In situ self-adaptive growth of graphene coatings on hard substrates via competitive NiCo catalysis reaction, Carbon 216 (2024).
[5] H. Wang, Z. Lin, B. Qin, J. Sun, F. Su, Z. Liang, Y. Zhang, High-temperature wear resistance improvement mechanism of TiAlCrNiSiNbx high-entropy alloy films through sliding wear-induced gradient nanostructure, Tribol. Int. 196 (2024).
[6] S. Fan, Y. Chen, J. Wu, S. Xiao, G. Chen, P.K. Chu, Structure, superlubricity, applications, and chemical vapor deposition methods of graphene solid lubricants, Tribol. Int. 198 (2024).
[7] A.M. Kumar, M.A. Ehsan, R.K. Suleiman, R.V.V.R. Murthy, B.A. Ahmed, M. Javid, Bimetallic CuNi Alloy Coatings on SS304 Substrate for Bipolar Plates of Proton Exchange Membrane Fuel Cells, ACS Appl. Energ. Mater. 7 (11) (2024) 4879–4890.
[8] J.L. Trompette, The comparative breakdown of passivity of tin by fluorides and chlorides interpreted through the 'law of matching affinities' concept, Corros. Sci. 94 (2015) 288–293.
[9] H. Dai, S. Shi, L. Yang, C. Guo, X. Chen, Recent progress on the corrosion behavior of metallic materials in HF solution, Corros. Rev. 39 (4) (2021) 313–337.
[10] K.D. Collins, G.W. Neilson, J.E. Enderby, Ions in water: Characterizing the forces that control chemical processes and biological structure, Biophys. Chem. 128 (2–3) (2007) 95–104.
[11] K.D. Collins, Ions from the Hofmeister series and osmolytes: effects on proteins in solution and in the crystallization process, Methods 34 (3) (2004) 300–311.
[12] S. Wang, Z. Zhang, W. Qian, Y. Yu, Y. Chen, Q. Zhao, Y. Zhang, H. Li, Y. Zhao, Enhancing corrosion resistance of AZ91D alloy through yttria-stabilized tetragonal zirconia (YSTZ)/MgO repaired ceramic coating with improved embrittlement cracking, Corros. Sci. 225 (2023).
[13] H. Zhang, C. Man, C. Dong, L. Wang, W. Li, D. Kong, L. Wang, X. Wang, The corrosion behavior of Ti6Al4V fabricated by selective laser melting in the artificial saliva with different fluoride concentrations and pH values, Corros. Sci. 179 (2021).
[14] C. Yang, C.Y. Wang, Z. Shen, L.P. Zhou, L.Y. Sheng, D.K. Xu, Y.F. Zheng, P.K. Chu, S. Xiao, T. Ying, X.Q. Zeng, Simultaneous improvement of wear and corrosion resistance of microarc oxidation composite coatings on ZK61 Mg alloy by doping with ZrO_2 nanoparticles, J. Mater. Sci. Technol. 224 (2025) 312–327.
[15] A.M. Zhang, C.B. Liu, P.S. Sui, C. Sun, L.Y. Cui, B. Kannan, R.C. Zeng, Corrosion resistance and mechanisms of smart micro-arc oxidation/epoxy resin coatings on AZ31 Mg alloy: Strategic positioning of nanocontainers, J. Magnes. Alloy. 11 (12) (2023) 4562–4574.
[16] R. Wang, C. Zhao, Z. Peng, X. Yan, Y. Sun, Q. Yu, B. Yu, M. Cai, F. Zhou, Corrosion and wear resistant polyp-xylene composite coating on AZ31 magnesium alloy prepared by micro-arc oxidation and vapor deposition, Prog. Org. Coat. 186 (2024).
[17] C. Yang, Z.M. Sun, C.Y. Wang, A.H. Huang, T. Ying, L.P. Zhou, Z.S. Ye, S. Xiao, P. K. Chu, X.Q. Zeng, A self-sealing and self-healing MAO corrosion-resistant coating on aluminum alloy by in situ growth of $CePO_4/Al_2O_3$, Corros. Sci. 245 (2025) 112706.
[18] Q. Mo, G. Qin, W. Wei, Z. Zhang, W. Li, Hydrophobic composite layers for enhancing long-term corrosion resistance of Al alloy micro-arc oxidation coating, Surf. Coat. Technol. 450 (2022).
[19] X. Qi, J. Li, Y. He, Y. Liu, R. Liu, R. Song, Study on the wear resistance and corrosion behaviour of self-sealed MAO/ZrO_2 coatings prepared on 7075 aluminium alloy, J. Alloy. Compd. 969 (2023).
[20] C. Yang, L. Sheng, C. Zhao, D. Wu, Y. Zheng, Regulating the ablation of nanoparticle-doped MAO coating on Mg alloy by MgF_2 passivation layer construction, Mater. Lett. 355 (2024).
[21] Z. Zheng, S. Wang, J. Long, J. Wang, K. Zheng, Effect of rare earth elements on high temperature oxidation behaviour of austenitic steel, Corros. Sci. 164 (2020).
[22] K. Xu, C. Zhan, M. Lou, X. Xiao, R. Zhou, F. Wang, X. Hu, Y. Yuan, K. Chang, Design of the rare-earth-containing materials based on the micro-alloying phase equilibria, phase diagrams and phase transformations, J. Mater. Sci. Technol. 151 (2023) 119–149.
[23] D. Fan, X. Zhong, Z. Zhang, P. Liu, L. Huang, Y. Niu, L. Wang, Q. Li, X. Zheng, Interaction of high-entropy rare-earth monosilicate environmental barrier coatings subjected to corrosion by calcium-magnesium-alumino-silicate melts, Corros. Sci. 207 (2022).
[24] T. Chen, Y. He, Y. Pan, K. Wang, M. Huang, L. Xue, Y. Li, F. Yang, Y. Zhou, H. Chen, High-entropy rare earth stannate ceramics: Acid corrosion resistant radiative cooling materials with high atmospheric transparency window emissivity and high near-infrared solar reflectivity, J. Adv. Ceram. 13 (5) (2024) 630–640.
[25] F.M. Draber, J.R. Denninger, P.C. Muller, I.K. Sommerfeld, M. Martin, The Impact of Nanoscale Percolation in Yttrium-Doped $BaZrO_3$ on the Oxygen Ion and Proton Conductivities: A Density Functional Theory and Kinetic Monte Carlo Study, Adv. Energy Sustain. Res. (2022).
[26] N. Tarasova, A. Galisheva, I. Animitsa, I. Anokhina, A. Gilev, P. Cheremisina, Novel mid-temperature $Y^{3+} \rightarrow In^{3+}$ doped proton conductors based on the layered perovskite $BaLaInO_4$, Ceram. Int. 48 (11) (2022) 15677–15685.
[27] X. Ma, S. Jin, R. Wu, Q. Ji, L. Hou, B. Krit, S. Betsofen, Influence alloying elements of Al and Y in Mg-Li alloy on the corrosion behavior and wear resistance of microarc oxidation coatings, Surf. Coat. Technol. 432 (2022).
[28] Z. Nie, H. Lu, Q. Liu, G. Chai, Y. Ding, G. Xu, J. Guo, Effect of copper introduction on the properties of micro-arc oxidation coating on powder metallurgy aluminum disk, Surf. Coat. Technol. 479 (2024).
[29] B. Delley, An all-electron numerical method for solving the local density functional for polyatomic molecules, J. Chem. Phys. 92 (1) (1990) 508–517.
[30] C. Perdew, Vosko, Jackson, Pederson, Singh, Fiolhais, Erratum: Atoms, molecules, solids, and surfaces: Applications of the generalized gradient approximation for exchange and correlation, Phys. Rev. B-Condens Matter 48 (7) (1993) 4978.
[31] S. Grimme, Semiempirical GGA-type density functional constructed with a long-range dispersion correction, J. Comput. Chem. 27 (15) (2006) 1787–1799.
[32] Y. Gao, Y. Chen, S. Xiao, T. Li, H. Wu, X. Meng, W. Li, S. Fan, Z. Ye, G. Chen, P. K. Chu, Effects and mechanism of Zn on the structure and corrosion resistance of microarc oxidation coatings on aluminum alloy, Appl. Surf. Sci. 659 (2024).
[33] J.J. Carey, M. Legesse, M. Nolan, Low Valence Cation Doping of Bulk Cr_2O_3: Charge Compensation and Oxygen Vacancy Formation, J. Phys. Chem. C 120 (34) (2016) 19160–19174.
[34] C. Yang, P. Chen, W. Wu, L. Sheng, Y. Zheng, P.K. Chu, A Review of Corrosion-Resistant PEO Coating on Mg Alloy, Coatings 14 (4) (2024).
[35] F.J. Burger, J.C. Wu, Dielectric breakdown in electrolytic capacitors, J. Electrochem. Soc. 118 (12) (1971) 2039–2042.
[36] J. Martin, P. Leone, A. Nomine, D. Veys-Renaux, G. Henrion, T. Belmonte, Influence of electrolyte ageing on the Plasma Electrolytic Oxidation of aluminium, Surf. Coat. Technol. 269 (2015) 36–46.
[37] Z. Jamshidipour, M. Toorani, M. Aliofkhazraei, M. Mahdavian, Reducing damage extent of epoxy coating on magnesium substrate by Zr-enhanced PEO coating as an effective pretreatment, J. Magnes. Alloy. 11 (2) (2023) 641–656.
[38] C.K. Wang, H.L. Lu, X.H. Zheng, H.Y. Yang, B.W. Xue, F. Guo, Reduced Graphene Oxide Films to Enhance the Tribological Performance of Micro-arc Oxidation Coatings, ACS Appl. Nano Mater. 7 (11) (2024) 12631–12643.
[39] Z. Fan, Q. Liu, N. Tu, J. Chen, H. Lu, Investigation on the effect and growth mechanism of two-stage MAO coating, Tribol. Int. 190 (2023).
[40] X. Dai, L. Wu, W. Ci, W. Yao, Y. Yuan, Z. Xie, B. Jiang, J. Wang, A. Andrej, F. Pan, Dual self-healing effects of salicylate intercalated MgAlY-LDHs film in-situ grown on the micro-arc oxidation coating on AZ31 alloys, Corros. Sci. 220 (2023).
[41] S. Damyanova, I. Shtereva, B. Pawelec, L. Mihaylov, J.L.G. Fierro, Characterization of none and yttrium-modified Ni-based catalysts for dry reforming of methane, Appl. Catal. B-Environ. 278 (2020).
[42] S. Ji, Y. Weng, Z. Wu, Z. Ma, X. Tian, R.K.Y. Fu, H. Lin, G. Wu, P.K. Chu, F. Pan, Excellent corrosion resistance of P and Fe modified micro-arc oxidation coating on Al alloy, J. Alloy. Compd. 710 (2017) 452–459.
[43] X. Deng, Y. Wang, Y. Chen, Z. Cui, C. Shi, Yttrium-doped TiO_2 compact layers for efficient perovskite solar cells, J. Solid State Chem. 275 (2019) 206–209.
[44] Z. Hu, D. Chen, P. Yang, L. Yang, L. Qin, Y. Huang, X. Zhao, Sol-gel-processed yttrium-doped NiO as hole transport layer in inverted perovskite solar cells for enhanced performance, Appl. Surf. Sci. 441 (2018) 258–264.
[45] T. Mongstad, A. Thogersen, A. Subrahmanyam, S. Karazhanov, The electronic state of thin films of yttrium, yttrium hydrides and yttrium oxide, Sol. Energy Mater. Sol. Cells 128 (2014) 270–274.
[46] J. Wang, H. Lu, G. Xu, Z. Bai, Z. Peng, Effect of ultra accurate control of electrolyte temperature on the performance of micro arc oxidation ceramic coatings, Ceram. Int. 49 (20) (2023) 33236–33246.
[47] J.R. Galvele, Tafel's law in pitting corrosion and crevice corrosion susceptibility, Corros. Sci. 47 (12) (2005) 3053–3067.
[48] H. Wang, Y. Song, X. Chen, G. Tong, L. Zhang, Microstructure and corrosion behavior of PEO-LDHs-SDS superhydrophobic composite film on magnesium alloy, Corros. Sci. 208 (2022).
[49] C. Wang, J. Shen, F. Xie, B. Duan, X. Xie, A versatile dopamine-induced intermediate layer for polyether imides (PEI) deposition on magnesium to render robust and high inhibition performance, Corros. Sci. 122 (2017) 32–40.
[50] Y. Zuo, R. Pang, W. Li, J.P. Xiong, Y.M. Tang, The evaluation of coating performance by the variations of phase angles in middle and high frequency domains of EIS, Corros. Sci. 50 (12) (2008) 3322–3328.
[51] C. Yang, C. Wang, Z. Shen, L. Zhou, L. Sheng, D. Xu, Y. Zheng, P.K. Chu, S. Xiao, T. Ying, X. Zeng, Simultaneous improvement of wear and corrosion resistance of

microarc oxidation coatings on ZK61 Mg alloy by doping with ZrO_2 nanoparticles, J. Mater. Sci, Technol, 2024.
[52] M. Kaseem, S. Fatimah, N. Nashrah, Y.G. Ko, Recent progress in surface modification of metals coated by plasma electrolytic oxidation: Principle, structure, and performance, Prog. Mater. Sci. 117 (2021).
[53] X.L. Zhang, Z.H. Jiang, Z.P. Yao, Z.D. Wu, Electrochemical study of growth behaviour of plasma electrolytic oxidation coating on Ti_6Al_4V: Effects of the additive, Corros. Sci. 52 (10) (2010) 3465–3473.
[54] A. Sobolev, A. Valkov, A. Kossenko, I. Wolicki, M. Zinigrad, K. Borodianskiy, Bioactive Coating on Ti Alloy with High Osseointegration and Antibacterial Ag Nanoparticles, ACS Appl. Mater. Interfaces 11 (43) (2019) 39534–39544.
[55] K. Venkateswarlu, N. Rameshbabu, D. Sreekanth, M. Sandhyarani, A.C. Bose, V. Muthupandi, S. Subramanian, Role of electrolyte chemistry on electronic and in vitro electrochemical properties of micro-arc oxidized titania films on Cp Ti, Electrochim. Acta 105 (2013) 468–480.
[56] M. Montazeri, C. Dehghanian, M. Shokouhfar, A. Baradaran, Investigation of the voltage and time effects on the formation of hydroxyapatite-containing titania prepared by plasma electrolytic oxidation on Ti-6Al-4V alloy and its corrosion behavior, Appl. Surf. Sci. 257 (16) (2011) 7268–7275.
[57] H. Duan, C. Yan, F. Wang, Effect of electrolyte additives on performance of plasma electrolytic oxidation films formed on magnesium alloy AZ91D, Electrochim. Acta 52 (11) (2007) 3785–3793.
[58] M. Kaseem, T. Zehra, T. Hussain, Y.G. Ko, A. Fattah-alhosseini, Length Electrochemical response of MgO/Co_3O_4 oxide layers produced by plasma electrolytic oxidation and post treatment using cobalt nitrate, J. Magnes. Alloy. 11 (3) (2023) 1057–1073.
[59] C. Wang, M. Sun, C. Yang, H. Wang, J. Wang, L. Mao, Y. Yang, T. Ying, P.K. Chu, X. Zeng, Degradation behavior of pure Mg in the physiological medium and growth mechanism of surface corrosion product films, J. Magnes, Alloy, 2024.
[60] Y. Chen, X. Lu, C. Blawert, M.L. Zheludkevich, T. Zhang, F. Wang, Formation of self-lubricating PEO coating via in-situ incorporation of PTFE particles, Surf. Coat. Technol. 337 (2018) 379–388.
[61] H. Yang, L. Wu, B. Jiang, W. Liu, J. Song, G. Huang, D. Zhang, F. Pan, Clarifying the roles of grain boundary and grain orientation on the corrosion and discharge processes of α-Mg based Mg-Li alloys for primary Mg-air batteries, J. Mater. Sci. Technol. 62 (2021) 128–138.
[62] G. Zhang, L. Wu, A. Tang, X.-B. Chen, Y. Ma, Y. Long, P. Peng, X. Ding, H. Pan, F. Pan, Growth behavior of MgAl-layered double hydroxide films by conversion of anodic films on magnesium alloy AZ31 and their corrosion protection, Appl. Surf. Sci. 456 (2018) 419–429.
[63] G. Brug, A.L. van den Eeden, M. Sluyters-Rehbach, J.H. Sluyters, The analysis of electrode impedances complicated by the presence of a constant phase element, J. Electroanal. Chem. Interf. Electrochem 176 (1984) 275–295.
[64] P. Fernandez-Lopez, S.A. Alves, I. Azpitarte, J.T. San-Jose, R. Bayon, Corrosion and tribocorrosion protection of novel PEO coatings on a secondary cast Al-Si alloy: Influence of polishing and sol-gel sealing, Corros. Sci. 207 (2022).
[65] K. Qian, C. Wang, M. Yang, X. Zou, Y. Zhang, Q. Dong, X. Wang, Y. Shao, Z. Cheng, J. Ju, C. Chu, Q. Chen, F. Xue, J. Bai, Self-assembly Zn-containing layer on PEO-coated Mg with enhanced corrosion resistance, antibacterial activity, and osteogenic property, Corros. Sci. 226 (2024).
[66] M. Toorani, M. Aliofkhazraei, R. Naderi, Ceria-embedded MAO process as pretreatment for corrosion protection of epoxy films applied on AZ31-magnesium alloy, J. Alloy. Compd. 785 (2019) 669–683.
[67] M. Toorani, M. Aliofkhazraei, R. Naderi, M. Golabadi, A.S. Rouhaghdam, Role of lanthanum nitrate in protective performance of PEO/epoxy double layer on AZ31 Mg alloy: Electrochemical and thermodynamic investigations, J. Ind. Eng. Chem. 53 (2017) 213–227.
[68] W. Tian, X. Zhang, Y. Guo, C. Mu, P. Zhou, L. Yin, L. Zhang, L. Zhang, H. Lu, X. Jian, L. Deng, Hybrid silica-carbon bilayers anchoring on FeSiAl surface with bifunctions of enhanced anti-corrosion and microwave absorption, Carbon 173 (2021) 185–193.
[69] M. Kaseem, H.-C. Choe, The effect of in-situ reactive incorporation of MoOx on the corrosion behavior of Ti-6Al-4 V alloy coated via micro-arc oxidation coating, Corros. Sci. 192 (2021).
[70] E. Jia, H. Lu, G. Xu, B. Xue, C. Wang, G. Chai, H. Yang, J. Li, Polyvinyl alcohol/polyethylene glycol composite hydrogel parceling on aluminum: Toward more robust micro-arc oxidation coatings, Ceram. Int. 49 (8) (2023) 13081–13091.
[71] Q. Huang, Z. Wu, H. Wu, S. Ji, Z. Ma, Z. Wu, P. Chen, J. Zhu, R.K.Y. Fu, H. Lin, X. Tian, F. Pan, P.K. Chu, Corrosion behavior of ZnO-reinforced coating on aluminum alloy prepared by plasma electrolytic oxidation, Surf. Coat. Technol. 374 (2019) 1015–1023.
[72] Y. Zhao, Z. Qian, X. Ma, H. Chen, T. Gao, Y. Wu, X. Liu, Unveiling the Semicoherent Interface with Definite Orientation Relationships between Reinforcements and Matrix in Novel Al_3BC/Al Composites, Acs Appl. Mater. Interfaces 8 (41) (2016) 28194–28201.
[73] Z. Zhang, Z. Yang, W. Qian, Y. Chen, Y. Xu, X. Xu, Q. Zhao, H. Li, Y. Zhao, H. Zhan, Achieving enhanced toughness of a nanocomposite coating by lattice distortion at the variable metallic oxide interface, Mater. Des. 224 (2022).
[74] A. Polat, M. Makaraci, M. Usta, Influence of sodium silicate concentration on structural and tribological properties of microarc oxidation coatings on 2017A aluminum alloy substrate, J. Alloy. Compd. 504 (2) (2010) 519–526.
[75] Y. Ding, H. Lu, G. Chai, L. Gao, High concentration of organic solvents in aluminum MAO: A study of structural and tribological property, J. Alloy. Compd. 981 (2024).
[76] Y. Cheng, Z. Peng, X. Wu, J. Cao, P. Skeldon, G.E. Thompson, A comparison of plasma electrolytic oxidation of Ti-6Al-4V and Zircaloy-2 alloys in a silicate-hexametaphosphate electrolyte, Electrochim. Acta 165 (2015) 301–313.
[77] L.O. Snizhko, A.L. Yerokhin, A. Pilkington, N.L. Gurevina, D.O. Misnyankin, A. Leyland, A. Matthews, Anodic processes in plasma electrolytic oxidation of aluminium in alkaline solutions, Electrochim. Acta 49 (13) (2004) 2085–2095.
[78] R.O. Hussein, X. Nie, D.O. Northwood, An investigation of ceramic coating growth mechanisms in plasma electrolytic oxidation (PEO) processing, Electrochim. Acta 112 (2013) 111–119.
[79] D.-D. Wang, X.-T. Liu, Y.-K. Wu, H.-P. Han, Z. Yang, Y. Su, X.-Z. Zhang, G.-R. Wu, D.-J. Shen, Evolution process of the plasma electrolytic oxidation (PEO) coating formed on aluminum in an alkaline sodium hexametaphosphate $((NaPO_3)_6)$ electrolyte, J. Alloy. Compd. 798 (2019) 129–143.
[80] S.M. Moon, S.I. Pyun, The formation and dissolution of anodic oxide films on pure aluminium in alkaline solution, Electrochim. Acta 44 (14) (1999) 2445–2454.
[81] S. Moon, Y. Jeong, Generation mechanism of microdischarges during plasma electrolytic oxidation of Al in aqueous solutions, Corros. Sci. 51 (7) (2009) 1506–1512.
[82] Z. Li, Q. Ren, X. Wang, Q. Kuang, D. Ji, R. Yuan, X. Jing, Effect of phosphate additive on the morphology and anti-corrosion performance of plasma electrolytic oxidation coatings on magnesium-lithium alloy, Corros. Sci. 157 (2019) 295–304.
[83] D.-D. Wang, X.-T. Liu, Y. Wang, Q. Zhang, D.-L. Li, X. Liu, H. Su, Y. Zhang, S.-X. Yu, D. Shen, Role of the electrolyte composition in establishing plasma discharges and coating growth process during a micro-arc oxidation, Surf. Coat. Technol. 402 (2020).
[84] C. Wang, H. Lu, H. Yang, B. Xue, E. Jia, G. Chai, The effect of adding polyethylene glycol to electrolyte solution on micro-arc oxidation coating on pure aluminum, Appl. Surf. Sci. 599 (2022).
[85] R. Nelson, C. Ertural, J. George, V.L. Deringer, G. Hautier, R. Dronskowski, LOBSTER: Local orbital projections, atomic charges, and chemical-bonding analysis fromprojector-augmented-wave-baseddensity-functional theory, J. Comput. Chem. 41 (21) (2020) 1931–1940.
[86] Q. Hao, P. Li, J. Liu, J. Huang, W. Zhang, Bandgap engineering of high mobility two-dimensional semiconductors toward optoelectronic devices, J. Materiomics 9 (3) (2023) 527–540.
[87] N. Zakay, A. Schlesinger, U. Argaman, L. Nguyen, N. Maman, B. Koren, M. Ozeri, G. Makov, Y. Golan, D. Azulay, Electrical and Optical Properties of ?-SnSe: A New Ultra-narrow Band Gap Material, ACS Appl. Mater. Interfaces 15 (12) (2023) 15668–15675.
[88] B. Krishnamurthy, R.E. White, H.J. Ploehn, Non-equilibrium point defect model for time-dependent passivation of metal surfaces, Electrochim. Acta 46 (22) (2001) 3387–3396.
[89] H. Yan, J.C. Wang, C. Meng, X. Wang, S.J. Song, X.Q. Fan, L. Zhang, H. Li, W. Li, M.H. Zhu, Towards long-term corrosion and wear protection of Al alloy: Synergy of $Ti_3C_2T_x$ flake and micro-arc oxidation coating, Corros. Sci. 174 (2020).
[90] L. Wen, Y.M. Wang, Y. Zhou, J.H. Ouyang, L.X. Guo, D.C. Jia, Corrosion evaluation of microarc oxidation coatings formed on 2024 aluminium alloy, Corros. Sci. 52 (8) (2010) 2687–2696.
[91] M. Mahinroosta, A. Allahverdi, Pilot-scale valorization of hazardous aluminum dross into γ-Al_2O_3 nanoadsorbent for efficient removal of fluoride, Environ. Technol. Innov. 23 (2021).
[92] A.V. Dolganov, V.D. Revin, S.G. Kostryukov, V.V. Revin, G. Yang, Kinetic and Thermodynamic Characteristics of Fluoride Ions Adsorption from Solution onto the Aluminum Oxide Nanolayer of a Bacterial Cellulose-Based Composite Material, Polymers 13 (19) (2021).
[93] Z. Shen, J. Jin, J. Fu, M. Yang, F. Li, Anchoring Al- and/or Mg-oxides to magnetic biochars for Co-uptake of arsenate and fluoride from water, J. Environ. Manage. 293 (2021).
[94] X. Chen, L. Xu, L.-L. Liu, L.-S. Zhao, C.-P. Chen, Y. Zhang, X.-C. Wang, Adsorption of formaldehyde molecule on the pristine and transition metal doped graphene: First-principles study, Appl. Surf. Sci. 396 (2017) 1020–1025.
[95] J. Martin, A. Melhem, I. Shchedrina, T. Duchanoy, A. Nominé, G. Henrion, T. Czerwiec, T. Belmonte, Effects of electrical parameters on plasma electrolytic oxidation of aluminium, Surf. Coat. Technol. 221 (2013) 70–76.
[96] C. Man, C. Dong, Z. Cui, K. Xiao, Q. Yu, X. Li, Characterization of the Outer Layer Nanostructure in the Electrochemical Response of Stainless Steel in Aqueous Sodium Hydroxide, Anal. Lett. 51 (9) (2018) 1384–1399.
[97] D.D. Macdonald, The history of the Point Defect Model for the passive state: A brief review of film growth aspects, Electrochim. Acta 56 (4) (2011) 1761–1772.
[98] X. Rong, X. Zhang, D. Zhao, C. He, C. Shi, E. Liu, N. Zhao, In-situ Al_2O_3-Al interface contribution towards the strength-ductility synergy of Al-CuO composite fabricated by solid-state reactive sintering, Scr. Mater. 198 (2021).
[99] A.J. Vattre, M.J. Demkowicz, Determining the Burgers vectors and elastic strain energies of interface dislocation arrays using anisotropic elasticity theory, Acta Mater. 61 (14) (2013) 5172–5187.
[100] X. Zhang, X. Cheng, Y. Si, J. Yu, B. Ding, Elastic and highly fatigue resistant ZrO_2-SiO_2 nanofibrous aerogel with low energy dissipation for thermal insulation, Chem. Eng. J. 433 (2022).

[101] F. Zhang, G. Zhang, L. Yang, Y. Zhou, Y. Du, Thermodynamic modeling of $YO_{1.5}$-$TaO_{2.5}$ system and the effects of elastic strain energy and diffusion on phase transformation of $YTaO_4$, J. Eur. Ceram. Soc. 39 (15) (2019) 5036–5047.
[102] P. Wang, Y. Bu, J. Liu, Q. Li, H. Wang, W. Yang, Atomic deformation mechanism and interface toughening in metastable high entropy alloy, Mater. Today 37 (2020) 64–73.
[103] M. Liao, P. Nicolini, L. Du, J. Yuan, S. Wang, H. Yu, J. Tang, P. Cheng, K. Watanabe, T. Taniguchi, L. Gu, V.E.P. Claerbout, A. Silva, D. Kramer, T. Polcar, R. Yang, D. Shi, G. Zhang, Ultra-low friction and edge-pinning effect in large-lattice-mismatch van der Waals heterostructures, Nat. Mater. 21 (1) (2022) 47-+.